Journal of Volcanology and Geothermal Research 327 (2016) 99–115

Contents lists available at ScienceDirect

Journal of Volcanology and Geothermal Research

journal homepage: www.elsevier.com/locate/jvolgeores

Phreatomagmatic and water-influenced Strombolian eruptions of a small-volume parasitic cone complex on the southern ringplain of Mt. Ruapehu, New Zealand: Facies architecture and eruption mechanisms of the Ohakune Volcanic Complex controlled by an unstable fissure eruption

S. Kósik [a,*], K. Németh [a], G. Kereszturi [a], J.N. Procter [a], G.F. Zellmer [a], N. Geshi [b]

[a] Volcanic Risk Solutions, Institute of Agriculture and Environment, Massey University, Turitea Campus, Palmerston North, New Zealand
[b] Geological Survey of Japan, AIST, Tsukuba, Ibaraki, Japan

ARTICLE INFO

Article history:
Received 12 April 2016
Received in revised form 13 July 2016
Accepted 18 July 2016
Available online 21 July 2016

Keywords:
Monogenetic
Phreatomagmatic and Strombolian eruption
Fissure vent
Tuff ring
DRE volume
Digital Terrain Model

ABSTRACT

The Ohakune Volcanic Complex is a late Pleistocene tuff ring – scoria/spatter cone complex located south of Ruapehu volcano. This small-volume volcano consists of an outer E-W elongated compound tuff ring edifice, three inner scoria-spatter cones and further volcanic depressions, located on the Ohakune Fault. We quantified accurately the variations of the eruptive styles and processes through time by systematic sampling of key stratigraphic marker beds at proximal and distal locations, and the determination of grain size distribution, componentry, density and vesicularity. Using a Digital Terrain Model coupled with stratigraphic data, we also determined the spatial distribution and volume of each identified unit and individual edifices within the Ohakune Volcanic Complex. Activity began with a shallow phreatomagmatic phase characterized by an almost continuous generation of a low eruptive column, accompanied by wet pyroclastic density currents, together with the ejection of juvenile fragments and accidental lithics from the surrounding country rocks. Subsequent activity was dominated by a variety of Strombolian eruptions exhibiting differing intensities that were at times disrupted by phreatic blasts or phreatomagmatic explosions due to the interaction with external water and/or sudden changes in magma discharge rate. At least three major vent-shifting events occurred during the eruption, which is demonstrated by the truncation of the initial tuff ring and the infilling of the truncated area by several coarse grained surge units. Our study indicates that approx. 12×10^6 m^3 DRE magma erupted within maximum 2.5 to 5 months through multiple vents. The erupted magma ascended from a depth of 16–18 km, and reached the surface within approximately 50 h. Alternating eruption styles, frequent vent-shifting and a variety of emplacement mechanisms inferred from the deposits of the Ohakune Volcanic Complex demonstrate the unpredictable nature of small-volume volcanism, contributing to our understanding of hazards attributed to this type of activity. Future small-volume eruptions within the Taupo Volcanic Zone may be of similar nature.

1. Introduction

Monogenetic (or small-volume) basaltic volcanoes occur within every geodynamic regime of the Earth and their associated volcanism is characterized by a range of eruption styles, eruptive materials and geomorphology (Sheridan and Wohletz, 1983; Lorenz, 1986; Head and Wilson, 1989; Valentine and Gregg, 2008; Németh, 2010; White and Ross, 2011; Kereszturi and Németh, 2012; Németh and Kereszturi, 2015). The determining factor of the eruptive behaviour of a volcano and the resulting volcanic products is the type of magma fragmentation (Lorenz, 1973; Walker, 1973; Kokelaar, 1983; Parfitt, 2004). Magmatic or dry fragmentation is characterized by exsolution and quick expansion of initially dissolved volatiles (e.g. H_2O and CO_2). The ascending bubbles coalesce and collapse near the surface and the exiting gas bursts result in Strombolian or Hawaiian eruptions (Parfitt, 2004; Houghton and Gonnermann, 2008; Valentine and Gregg, 2008). The main differences between these two eruptive styles are the speed of the gas flux with respect to magma rise (Parfitt, 2004) and differences between the ejection mechanisms of fragments during eruptions (e.g. the duration of particles remaining as ballistics is greater in Strombolian eruptions, and particles transported by fallout jets is more common in Strombolian activity) (Riedel et al., 2003; Capaccioni and Cuccoli, 2005). Hawaiian eruptions exhibit higher magma flux that allows limited cooling within the fire-

* Corresponding author.
E-mail address: s.kosik@massey.ac.nz (S. Kósik).

http://dx.doi.org/10.1016/j.jvolgeores.2016.07.005
0377-0273/

fountain, which results in agglutination or fusing due to the high accumulation rate of the fragments (Head and Wilson, 1989), while the clasts from Strombolian eruptions cool prior to landing (Walker, 1973; Vergniolle and Mangan, 2000). Hydromagmatic or wet fragmentation refers to the interaction of magma and external water resulting in the conversion of magmatic heat to mechanical energy (Sheridan and Wohletz, 1983; Lorenz, 1985; Wohletz, 1986; White, 1996; Wohletz and Zimanowski, 2000; Lorenz, 2003; Kereszturi and Németh, 2012). The interaction and the resulting volcanic processes in most cases primarily depend on the water/magma ratio, lending to two basic types of fragmentation: phreatomagmatic (Taalian) and Surtseyan (Kokelaar, 1983; Wohletz and Sheridan, 1983; White, 1996; Kereszturi and Németh, 2012). During Surtseyan-style eruptions the water/magma ratio is high enough (e.g. in a shallow subaqueous environment) to allow continuous bulk mixing and fragmentation. As a result, the Surtseyan-style eruptions are characterized by quickly recurring, short-lived tephra jets, causing the rapid growth of a volcanic pile and the growth of a tuff cone (Thorarinsson, 1965; Kokelaar and Durant, 1983). In contrast, phreatomagmatic eruptions are characterized by lower water/magma ratios in the subaerial environment, in which fragmentation is triggered by a molten fuel-coolant interaction (MFCI) process causing energetic thermohydraulic explosions (Sheridan and Wohletz, 1981; Wohletz, 1986; White, 1996; Wohletz and Zimanowski, 2000; Büttner et al., 2002). The phreatomagmatic eruptions commonly form two types of volcanoes, depending on the substrate (Lorenz, 2003; Auer et al., 2007) and the depth of excavation: tuff rings and maars. Both types have an ejecta ring around their craters, but in contrast with tuff rings, maar craters cut deeply into the pre-eruptive surface and are underlain by a mixture of volcanic and country rock fragments composed of debris commonly referred to as the diatreme (Wohletz and Sheridan, 1983; Martin and Németh, 2005; White and Ross, 2011; Kereszturi and Németh, 2012; Agustin-Flores et al., 2014). During phreatomagmatic eruptions the explosion loci often exhibit a downward or lateral migration according to the hydrologic and local substrate settings or following regional faults as it documented at Ukinrek Maars, Alaska (Kienle et al., 1980), Cerro Xalapaxco (Abrams and Siebe, 1994) and Tecuitlapa Maar (Ort and Carrasco-Núñez, 2009), central Mexico, Tihany maars (Németh et al., 2001), and Yangpori diatreme, SE Korea (Son et al., 2012). Newer models presume that MFCI occurs at varying depths within the diatreme during the course of the activity, although it is most effective at shallow depth, where the hydrostatic pressure is less than the critical pressure. Thus, deep-seated explosions are rarely powerful enough to erupt (Valentine and White, 2012; Graettinger et al., 2015). As commonly documented, longer-lived eruptions of subaerial volcanoes and scoria cones quickly deplete the water from the substrate or surface sources and gradually become dry explosive and/or effusive eruptions, such as Ság-hegy, western Hungary (Martin and Németh, 2004), Crosa de Sant Dalmai maar, NE Spain (Pedrazzi et al., 2014b), and Motukorea tuff ring, Auckland Volcanic Field, New Zealand (Agustín-Flores et al., 2015). An alternating pattern of phreatomagmatic and magmatic activity may also be exhibited due to vertical or lateral migration of eruption loci, providing new influx of water from distinct aquifers (e.g. Rothenberg volcano, East Eifel; Tihany maars, Hungary; Atexcac maar, eastern Mexico) (Houghton and Schmincke, 1986; Németh et al., 2001; Carrasco-Núñez et al., 2007), or due to change in magma flux as documented at White Island, New Zealand (Houghton and Nairn, 1991).

The Ohakune Volcanic Complex (OVC), North Island, New Zealand was previously examined by Houghton and Hackett (1984). Their study was based on the examination of outcrops in quarries that were cut into the scoria cones and the tuff rings. Since their work the extent of the main quarry has increased significantly, exposing a much larger internal portion of this small-volume volcano. The currently exposed volcanic units show evidence for new vent openings and simultaneous activity of distinct vents characterized by different eruption styles resulting in a very complicated volcanic architecture. Due to the continual influence of external water and the relatively small volume of magmatic eruptions in the final phases, volcanic features from the embryonic stage of the activity were not completely covered, making the OVC one of the few known locations that retains vital information on the evolution of monogenetic volcanoes affected by complex changes of vent loci (Houghton and Schmincke, 1989; Pedrazzi et al., 2014b; Agustín-Flores et al., 2015). Previous studies concentrated on the central vent volcanism and related hazards (e.g. Cronin et al., 2003; McClelland and Erwin, 2003; Graettinger et al., 2010; Pardo et al., 2012), rather than focussing on the hazards produced by such a volcanism within the Taupo Volcanic Zone (TVZ) in terms of eruption cloud height, eruptive volumes and potential longevity of an eruption. This study is the first step towards assessing the volcanic hazards associated with small-volume volcanism with respect to the relationship between parasitic/satellite volcanoes and their larger polygenetic counterparts of the TVZ. We focus on the understanding of the eruptive conditions including influencing factors of fragmentation, dominant eruptive and depositional mechanisms, the range of the eruptive products created by different eruptive styles and the preserved geochemical characteristics. Furthermore new Geographical Information Systems (GIS) techniques allow utilizing a high resolution Digital Terrain Models (DTM) in order to study the geomorphologic features, providing great support in the understanding of the temporal evolution of this monogenetic volcano and contributing to the identification of the hazards of future small-volume eruptions within the TVZ (Fig. 1).

2. Regional setting

The late Pleistocene monogenetic OVC (also known as Rochfort Crater) is located within the south-southwest ringplain of Ruapehu stratovolcano (Fig. 1). Volcanic activity in the southern end of the TVZ dates back to the eruption of Hauhungatahi volcano (Fig. 1), which has been dated at 921 ± 40 ky by $^{40}Ar/^{39}Ar$ (Cameron et al., 2010). This earliest activity was followed by the construction of primeval edifices of Ruapehu, which are mostly eroded and overlapped by the present Ruapehu volcano about 250 ky ago (Hackett and Houghton, 1989; Tost and Cronin, 2015). The OVC, along with another monogenetic volcano (Rangataua Craters), are the southernmost appearance of volcanic activity within the TVZ (Fig. 1) (Cole et al., 1986; Hackett and Houghton, 1989). The surrounding county rocks are mostly reworked volcanoclastic sediments of Mt. Ruapehu and andesitic to rhyolitic fallout tephra from various sources (Hackett and Houghton, 1989; Möbis, 2010). Pliocene marine sediments (mostly siltstones and sandstones of the Matemateaonga Formation) underlie the volcanic edifice and volcanoclastic series, and occasionally crop out as uplifted fault-bounded blocks (Townsend et al., 2008). The eruptions of the OVC are most likely linked to the E-W trending Ohakune Fault (Fig. 2) (Houghton and Hackett, 1984). The eruptions started in a flat or slightly sloping laharic depositional environment, where the unconsolidated reworked volcanoclastic sediments could have been divided by newly formed river pathways. The youngest sediments of the pre-eruptive surface sourced from the lavas of the 60–15 ky old Mangawhero Formation while the edifice is overlain with disconformity by the Kawakawa/Oruanui Tephra, which gives a 25.4 ka minimum age for the activity (Hackett and Houghton, 1989; Vandergoes et al., 2013). Radiocarbon dating on charred wood from an OVC associated coarse lapilli layer from a distal outcrop (Fig. 2) yields a date of 31,500 ± 300 y BP (Froggatt and Lowe, 1990).

3. Materials and methods

3.1. Field observations and sampling

The proximal sequence of the ejecta ring (outer edifice) was examined in terms of thickness, colour, bedding structures and grading, componentry and grain morphology. We also examined the distal sequence in order to correlate the existing units (Fig. 2). High resolution georeferenced thickness data of individual eruptive units from within

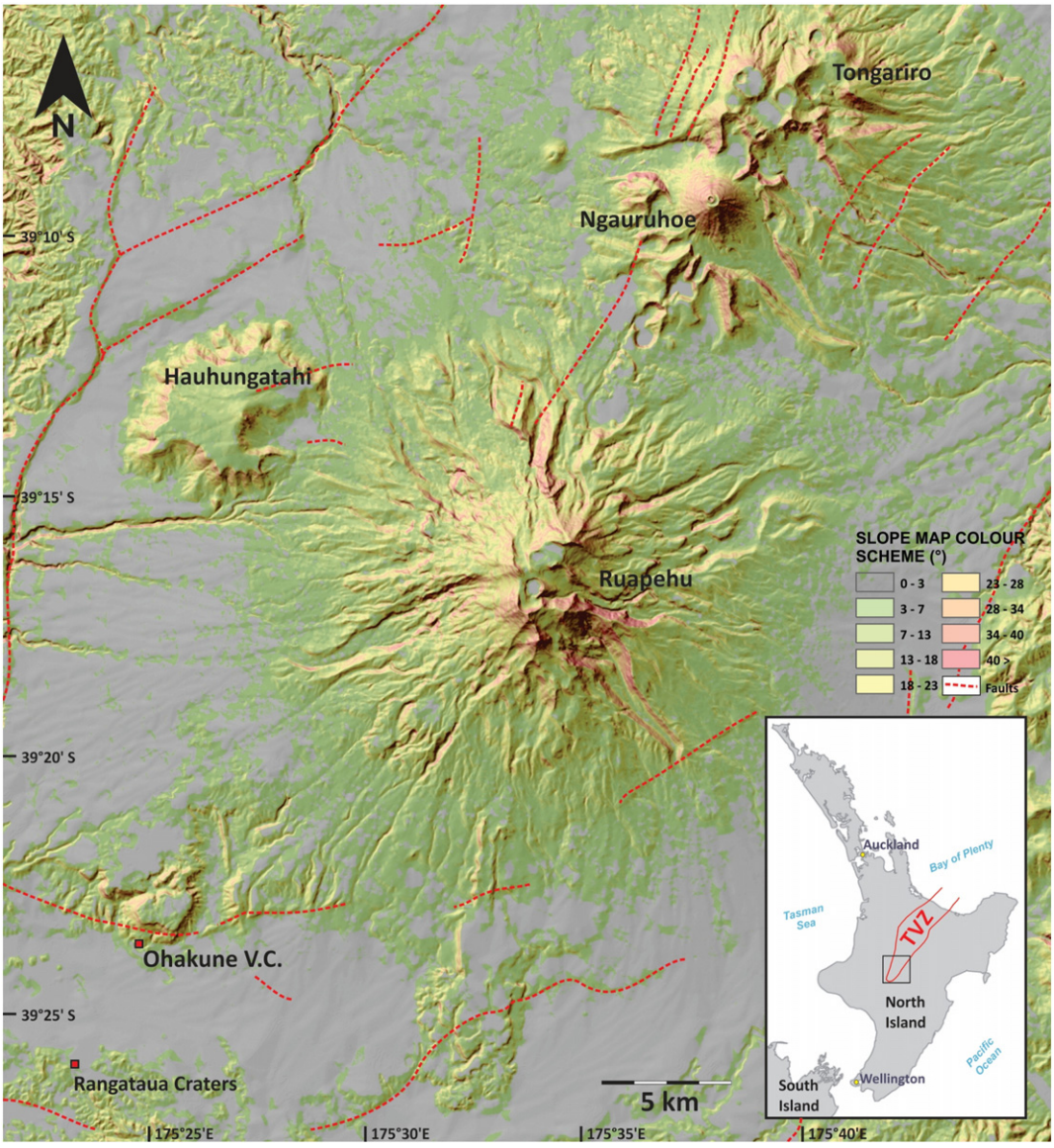

Fig. 1. Topography of the southern, dominantly andesitic part of Taupo Volcanic Zone (TVZ) as shown on shaded slope map derived from a 8 m DEM (LINZ - Land Information New Zealand, 2012). Inset map shows its geographic position within New Zealand.

the eastern ejecta ring were collected by Terrestrial Laser Scanner (TLS) (Fig. 2). The quarry walls were surveyed using approximately 15 mm point spacing at 30 m distance by TLS, along with high resolution photographs. The units named as A–E, G, H, I, K–M, O–Q and U (Fig. 2) were sampled from the proximal facies of the edifice within the quarry. In addition, large juvenile fragments (>10 cm in diameter) were collected from the massive ballistic beds (A, D, H, J, T, X) (Fig. 2) for density, petrography and geochemical analysis. The surface morphology of the ejecta ring was mapped using TLS and RTK GPS to upgrade remotely sensed Digital Terrain Model (DTM) (Gómez-Vasconcelos et al., 2016) for edifice volume and unit volume calculations.

3.2. Sample preparation and analytical techniques

The grain size distribution of the matrix supported units were defined using phi sizes from −5 ϕ (32 mm) to 4 ϕ (0.63 mm) at half phi intervals. Particles smaller than 4 ϕ were analysed by a Partica LA-950V2 Laser Scattering Particle Size Distribution Analyser at Massey University. Grain size parameters were calculated using the Gradistat 8.0 program (Folk and Ward, 1957; Walker, 1971; Blott and Pye, 2001). The componentry and the morphological characteristics of the fragments were examined at −3, 0.5 and 2 ϕ under a stereomicroscope and a FEI Quanta 200 environmental Scanning Electron Microscope (SEM). The majority of samples had to be cleaned in an ultrasonic bath in order to disaggregate the adhering fine material. The microscopic observations were complemented with point counting of stereomicroscopic images using the JMicroVision 1.2.7 software. Five subsamples of blocks and bombs from each of the bomb-bearing units (A, D, H, J, T, X) were examined to determine envelope densities and vesicularities, which was carried out using a Micrometrics GeoPyc 1360 analyser. We also measured the densities for 30–3 ϕ clast from A, D, K, M, P units. Vesicularity and clast microtextures of the blocks/bombs were determined using 2D macroscopic and SEM image analysis for 10 samples from 6 units (Table 1). Macroscopic high resolution images have been taken from each sample (with an extent of 40 to 60 cm^2) by a photo and document scanner (Canon Pixma MP160), while the smaller vesicles were mapped through backscattered electron imaging (BSE) of thin sections striving to the requirement of representativeness. Two macroscopic images and nine microscopic images were captured at 25× and 100× magnifications ensuring that the resolution was sufficient to capture all size ranges of bubbles with appropriate resolution. 2D vesicularity was measured using ImageJ and the Matlab™-based FOAMS (Fast Object Acquisition

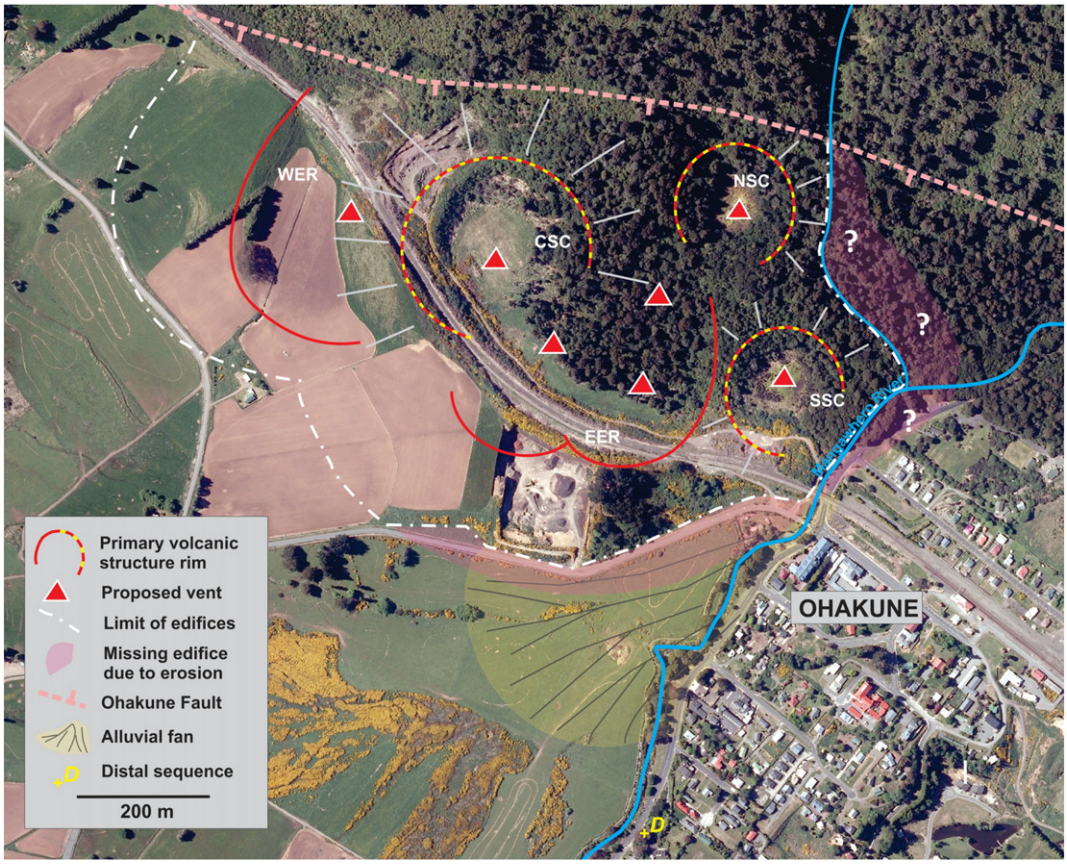

Fig. 2. Aerial photograph of OVC with its proposed architecture. The main edifices are labelled; West ejecta ring (WER), East ejecta ring (EER), Central scoria cone (CSC), South scoria cone (SSC), North scoria cone (NSC).

and Measurement System) software by the method of exponential image nesting (Shea et al., 2010). Applying stereological conversion of vesicles by FOAMS provided further details of vesicle textures (e.g. vesicle size and vesicle volume distributions), vesicle size and shape properties which preserve information on the eruptive conditions (e.g. bubble nucleation or degassing) (Shea et al., 2010). Geochemical compositions were determined for single ash particles from matrix-rich (A–E, G–I, L) units (Fig. 2) at the size of 0.5 ϕ with a JEOL JXA-840 Electron Microprobe Analyser (EMPA) equipped with a Princeton Gamma Tech Prism 2000 Si(Li) EDS X-ray detector at Massey University, employing an accelerating voltage of 15 kV and a 10 μm defocused beam. Groundmass glass of spatter bombs were analysed with defocused beam and olivine and pyroxene crystals of the scoriaceous fragments from the bomb beds (D, H, J, T, X units) with a focused beam by EMPA. Elemental analysis and mapping of thin sections was accomplished by energy dispersive x-ray spectroscope (EDAX) of SEM.

4. Architecture of Ohakune Volcanic Complex

The OVC has previously been described as a kilometre wide slightly elongated tuff ring with intra-crater scoria cones (Houghton and Hackett, 1984). Based on a DTM (Horizons Regional Council, 2016), aerial photo from 1951 and field observations, the northern section of the tuff ring appears undeveloped due to lack of space between the vents and the Ohakune fault scarp. Only scoriaceous beds are exposed at the eastern section of the edifice that correlate with the pyroclastic successions at higher stratigraphic levels (Figs. 2 and 3). Furthermore dense vegetation makes access difficult, and erosion by the Mangawhero River makes reconstruction difficult in this part of the volcanic complex. It appears that the southern section may also not be a single edifice, but rather consists of coalesced ejecta rings formed by alternating phreatomagmatic and Strombolian eruptions from separate vents (Figs. 2 and 3). For these reasons, the outer complex edifice is not an ordinary tuff ring (Lorenz, 1986; Kereszturi and Németh, 2012), and we will refer to it here as an ejecta ring. There are at least 5 depressions between the ejecta ring structures and the fault plain, which probably reflects the location of the eruptive vents that were active during the final eruptive phases (Fig. 2). Most of these pits form a 600 m long fissure zone subparallel with the Ohakune Fault, which may indicate that the area was penetrated by the extruding tips of a blade-like dyke. Three of the depressions host the craters of a large and two small late stage scoria/spatter cones (Fig. 2).

The proximal sequences of the inner and outer edifices are exposed at several quarries. The largest inner scoria/spatter edifice (CSC) (Figs. 2 and 3) has a bedded structure of coarse scoria and agglutinated scoria units, alternating with clastogenetic lava flow units (Fig. 3). The majority of the edifice of the scoria cone has been quarried away except the north section. The proximal sequence of the ejecta ring is very well exposed in a quarry that is currently active (Figs. 3 and 4); however the contact with the country rock is not visible (Fig. 4). Geomorphologic observations, coupled with Real-Time Kinematic (RTK) GPS measurements, showed that the pre-eruptive country rocks are located at the altitude of 585–590 m above sea level, thus about 10 m of the initial sequence has not yet been exposed. The lowest visible units are light-coloured and matrix-rich, while the upper units appear to be the scoria-dominated units alternating with units of pyroclastic density currents and poorly-sorted units of weathered scoriaceous fragments with denser lava blocks. The distal sequence comprises a 1.8-thick unit that is situated about 600 m south of the OVC on the left side of Mangawhero River (Fig. 2). The distal outcrops have been separated from the OVC

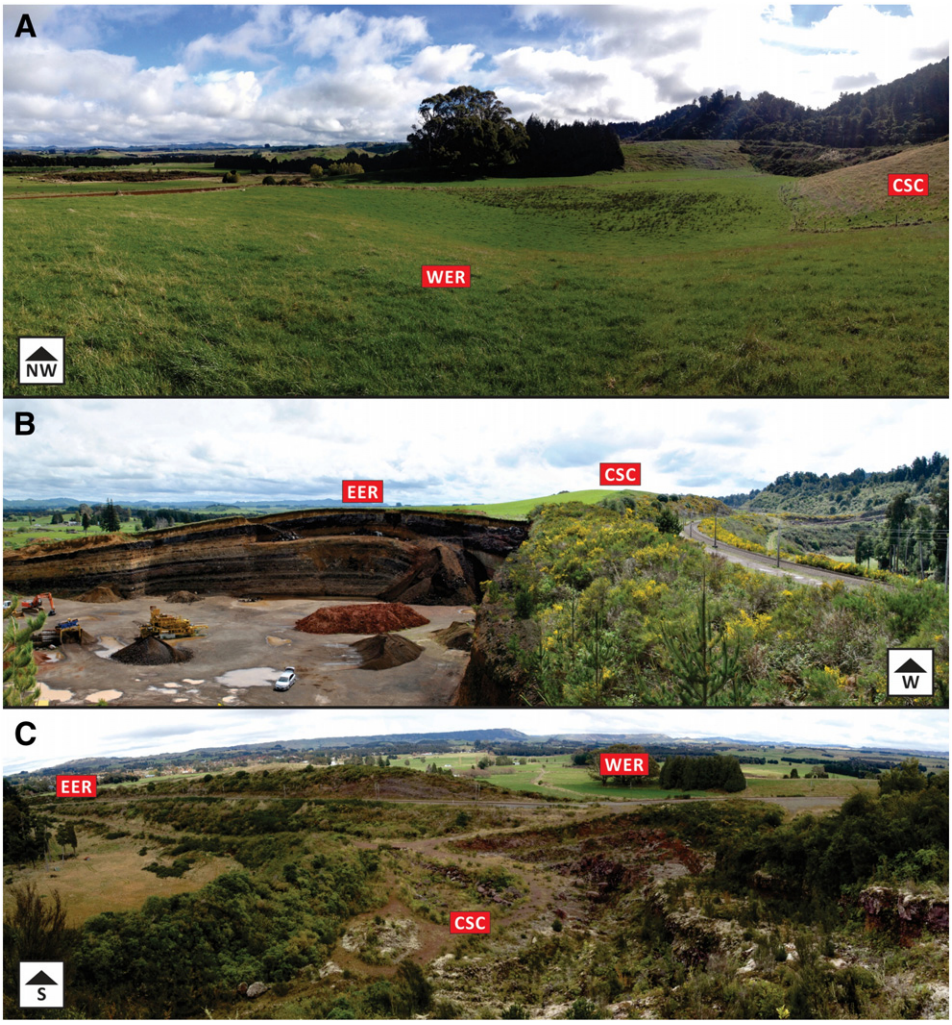

Fig. 3. Morphological features of OVC. A: View from the rim of WER to its crater floor. On the right edge the foot of the CSC partly fill in the crater. B: The quarried section of the coalesced EER and the rim of CSC. C: View from the highest part of the CSC to its crater floor (grassland) and its quarried interior of alternating welded and unwelded Strombolian (or Hawaiian) units. The railway line is also cut through the scoria cone and EER on the left and WER on the right.

by fluvial erosion prior to the Oruanui eruption (25.4 ky) and those deeply cut channels have been later occupied by fluvial sediments as part of the formation of an alluvial fan (Fig. 2).

5. Stratigraphy and sedimentology

The active quarry exposes the coalesced eastern ejecta ring (EER) (Figs. 2 and 3). The walls are north-west radially orientated to the ejecta ring, providing a proximal to distal cross-section of the volcano. At the NW corner of the quarry we identified an unconformity. In relation to the unconformity a small fault is also visible with decreasing offsets from the base to the top (Fig. 4). The lowest, barely exposed units are thick-bedded and poorly-sorted with accidental lithics from the laharic basement and dense lava fragments from the OVC eruption alternating with massive ash beds. The upper sequence of the ejecta ring is characterized by dark-coloured bomb beds alternating with light-coloured ash beds and mixed beds through the approximately 22 m thick visible succession. 95% of the fragments are clearly associated with the magma erupted from OVC, the most distinctive feature of which is the high content (10–15%) of pyroxene and olivine phenocrysts up to 0.8 cm in size. The deposited fine tephra at the OVC typically have a high amount of aggregates and dust-adhered fragments with a lack of accretionary lapilli (Fig. 5). The ash particles also display heterogeneity in terms of colour (dark to light brown), alteration, vesicularity, and shape (skeletal/irregular to blocky) (Fig. 5). The majority of the ash fragments are moderately vesicular similar to c-d textures (Fig. 5). There is an insignificant amount of accidental lithics in the finer grain size. Most of the lapilli and block fragments are dark-coloured dense or vesicular basaltic juveniles up to 25–30 cm. The remaining accessory fragments are mostly well-rounded andesitic boulders of the fluvial-laharic basement originated from Ruapehu and a small percentage of baked sedimentary rocks (Fig. 4). The exposed units were labelled (of Fig. 4) and classified into 4 lithofacies on the basis of sedimentological characters (e.g. componentry, grain size distribution and sedimentary structures) (Fig. 4); 1. **Ab**: ash beds (C, E, G, L, N, O, Q, S units), 2. **Ab$_C$**: ash beds with coarse fragments (A, I, U), 3. **Bb$_A$**: bomb beds with ash (B, D, H, K, P, R, X$_{Lower}$), 4. **Bb**: spatter-scoria bomb beds (J, M, T, X$_{Upper}$).

5.1. Ash beds (Ab)

5.1.1. Description

Ash beds are matrix-supported massive, diffusively stratified or planar bedded with internal low angle unconformities. The beds are poorly-sorted and predominantly composed of fresh and varying amounts of yellowish to brownish coloured palagonitized ash and lapilli fragments from −3 ϕ to 7 ϕ in size with a peak at 3.5 ϕ. Mud-coating is frequent on the surface of fragments. Some ash beds exhibit stratification by the alternation of finer and coarser layers, where the coarsest layers often show inverse grading (e.g O_1 layer). The tephra has a damp, adhesive behaviour, which is brightening after drying. Impact

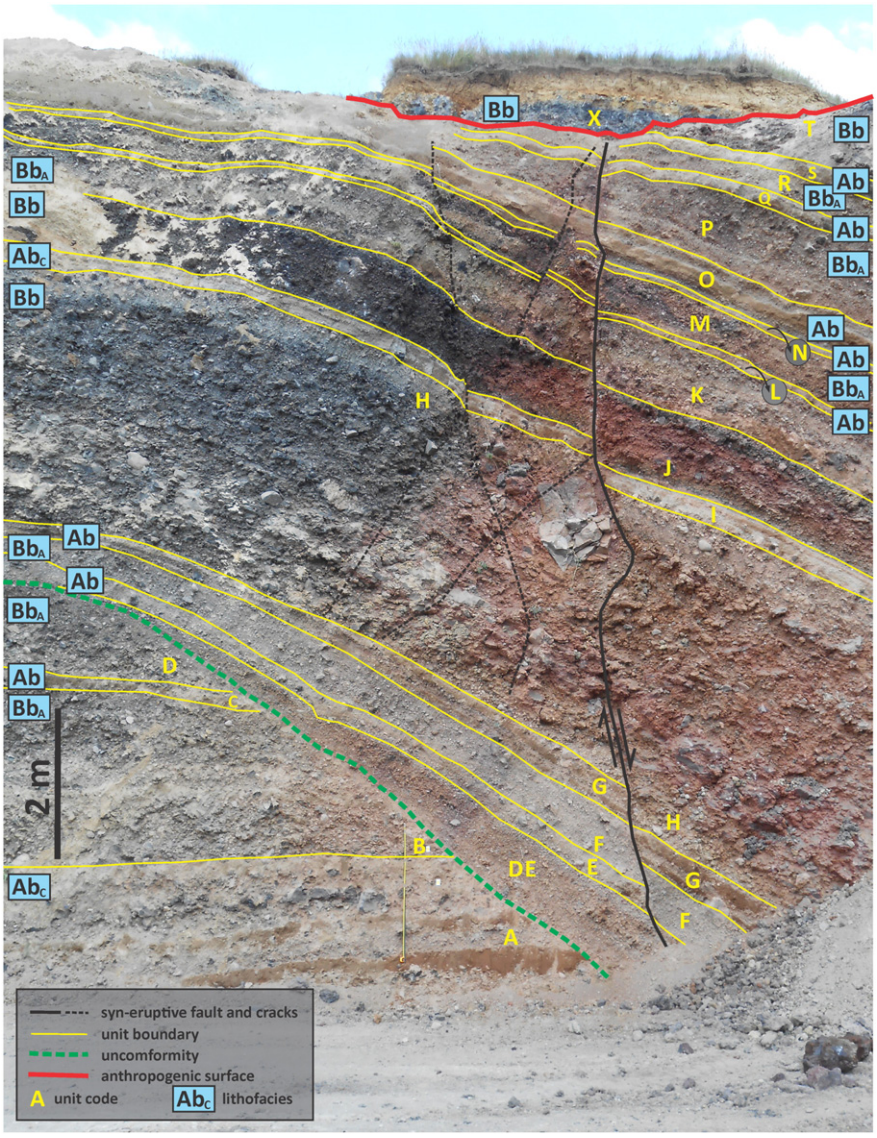

Fig. 4. Stratigraphic sequence of the proximal part of EER at the northwest corner of the quarry. This is one of the locations exhibits the opening of a new vent. Note the oxidation pattern of right hand side of the fault.

sags are rare. The biggest clasts (up to 20 cm) can be altered vesicular or dense scoriaceous fragments correlated to the Ohakune eruption and rounded andesite cobbles of Ruapehu origin. The thickness of the units is variable (≤50 cm thick), and visible single layers are in the range of 1 cm to 25 cm thick. Individual beds usually exhibit irregular thickness variations without appreciable thinning trends within the quarry (Fig. 4). The distal counterparts are mostly thinly stratified ash (−1 to 7 ϕ in size) with low angle cross and dune bedding structures. The distal sequence also exhibits soft sediment deformation and impact sags with ballistic bombs up to 10 cm in size.

5.1.2. Emplacement interpretation

The high proportion of mud-coated fragments and the wet and massive nature of beds imply an abundance of water during the eruptions and during deposition (Heiken and Wohletz, 1985; Sohn and Chough, 1989; Houghton and Smith, 1993). The clearly visible cross and dune bedding of the distal deposits confirms the dilute pyroclastic density current origin of these deposits. Palagonitized ash fragments and fine dust is probably derived from the slurry of the crater floor. Hence, minor recycling of juvenile fragments from the earlier products of the OVC activity must have occurred (Houghton and Smith, 1993; D'Oriano et al., 2014). The majority of coarser fragments are likely to have been transported by ballistic trajectories or in pyroclastic density currents at the proximal section, while the coarser fragments clearly have a ballistic origin at the distal sequence (Fisher and Schmincke, 1984; Sohn and Chough, 1989). Therefore, **Ab** units most likely deposited as a result of discrete phreatomagmatic explosions generating wet pyroclastic surges and some tephra fall.

5.2. Ash beds with coarse fragments (Ab_C)

5.2.1. Description

Ash beds with coarse fragments are matrix-supported, very poorly-sorted units with variable amounts of coarse lapilli and bomb size clasts (Fig. 6). The matrix is composed of fresh juvenile, mud-coated and palagonitized ash and medium lapilli fragments between −3 to 7 ϕ in size with the main peak at −2.5 to −1.5 ϕ. The larger sized lapilli and bombs are composed of rounded andesite cobbles and fresh olivine/pyroxene-bearing basaltic fragments up to 50 cm in size. Some of the lava fragments are vesicular with a dense core exhibiting conchoidal fractures, others have cauliflower or plastically deformed shapes. None of the clasts have formed visible impact sags. The fraction of

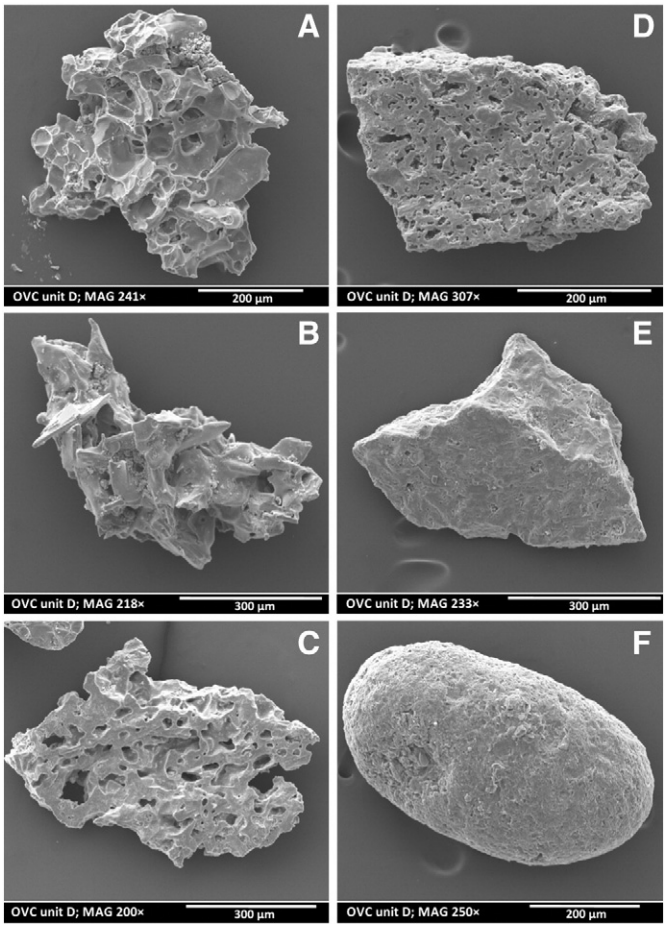

Fig. 5. SEM images of juvenile ash fragments characterized by high to low vesicularities (A–E) and a typical aggregate (F). Type a with spherical vesicles is extremely rare at OVC would represent Strombolian fragmentation (Heiken and Wohletz, 1985), type b with microlites is the most vesicular of the common fragments and might related to eruptions with minor influence by water/magma interaction, while c–e types might have more phreatomagmatic origin. By comparison, a block was smashed by hammer and the bits were similar to type-c fragments.

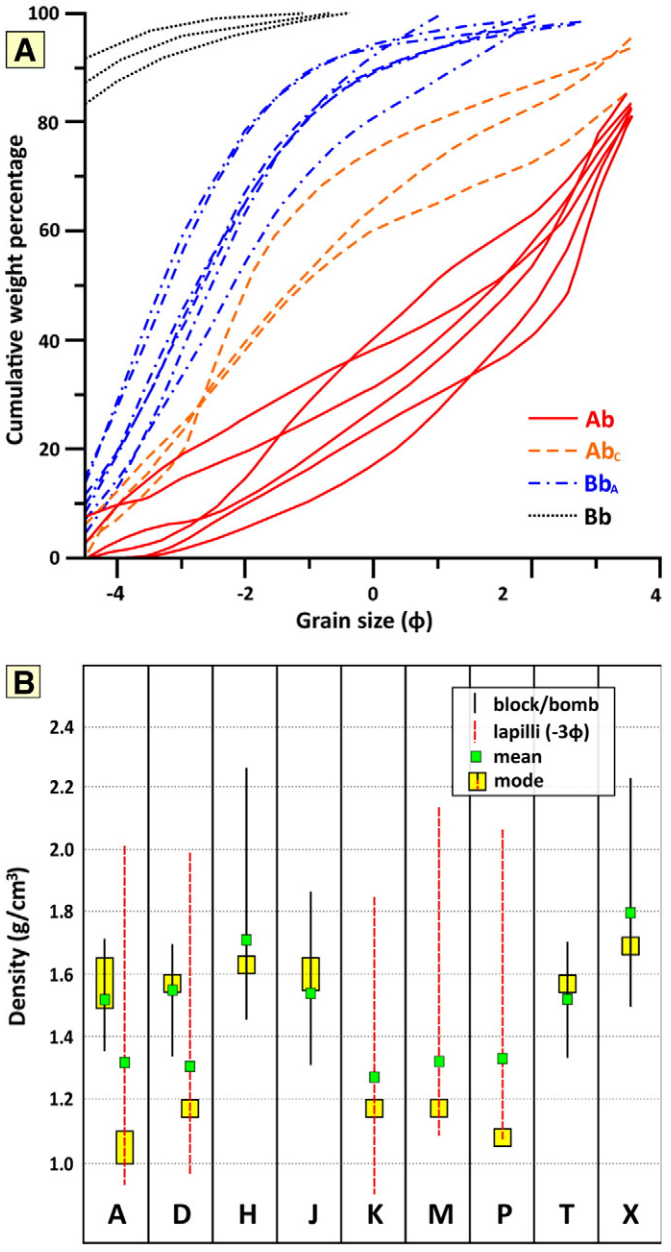

Fig. 6. A Cumulative grain size distribution of distinct units from the proximal sequence of EER. Bb unit distributions are only represent estimations based on field observations. B Density variations of bomb/block and lapilli (−3 ϕ) sized juvenile fragments from EER proximal sequence.

these larger clasts is significantly higher than in the **Ab** units. **Ab$_C$** units often have internal bedding without sharp depositional or erosional contacts. These units were typically interstratificated with subunits that are analogous to **Ab**-type lithofacies traverses through the outcrop (Fig. 4).

5.2.2. Emplacement interpretation

The lack of the sharp internal structures and impact sags suggest continuous deposition by fallout and debris jets, while the relatively coarse average size as well as the smaller portion of very fine (<3 ϕ) juvenile fragments imply less energetic fragmentation than in the Ab units. The massive beds of **Ab$_C$** interstratificated Ab beds may be the result of a sustained, but varying level of interaction of magma with external water at shallow depth, which enables a near-continuous discharge of tephra and gases coinciding with more energetic discrete explosions. The continuous uprush produced a complex deposition of fresh dry ash, recycled damp ash and aggregates from the contact zone of the dyke edge and conduit wall, similar to the 1976–1982 eruption of White Island, New Zealand (Houghton and Nairn, 1991). However, the fresh, sometimes plastically deformed bombs (in unit A) suggest that the middle part of the dyke could have produced drier Strombolian-type fragments occasionally. Strombolian/Hawaiian and phreatomagmatic eruptions usually represent very different types of magma fragmentation (Wohletz and McQueen, 1984), however there are a few documented eruptions that exhibit both fragmentation processes at the same time (Moore et al., 1966; Kienle et al., 1980; Dzurisin et al., 1995; Valentine et al., 2000). There are some alternative models for magma fragmentation and admixture of tephra from two contrasting eruptions. Depending on variations in vent geometry and hydrological conditions the products could have originated from different parts or depths of the same vent or fissure (Houghton and Schmincke, 1986; Dzurisin et al., 1995; Valentine and White, 2012) or from two or more localized vents along a fissure (Moore et al., 1966; Kienle et al., 1980; Pedrazzi et al., 2014a; Belousov et al., 2015). Alternatively, these units can be interpreted as products of a long-lasting transitional phase between phreatomagmatic and magmatic phases of Strombolian/Hawaiian eruption (Belousov et al., 2015), which might have been emplaced by spatter/scoria-bearing pyroclastic density currents (Valentine et al., 2000). One of the Ab$_C$-type units (U) is interfingering

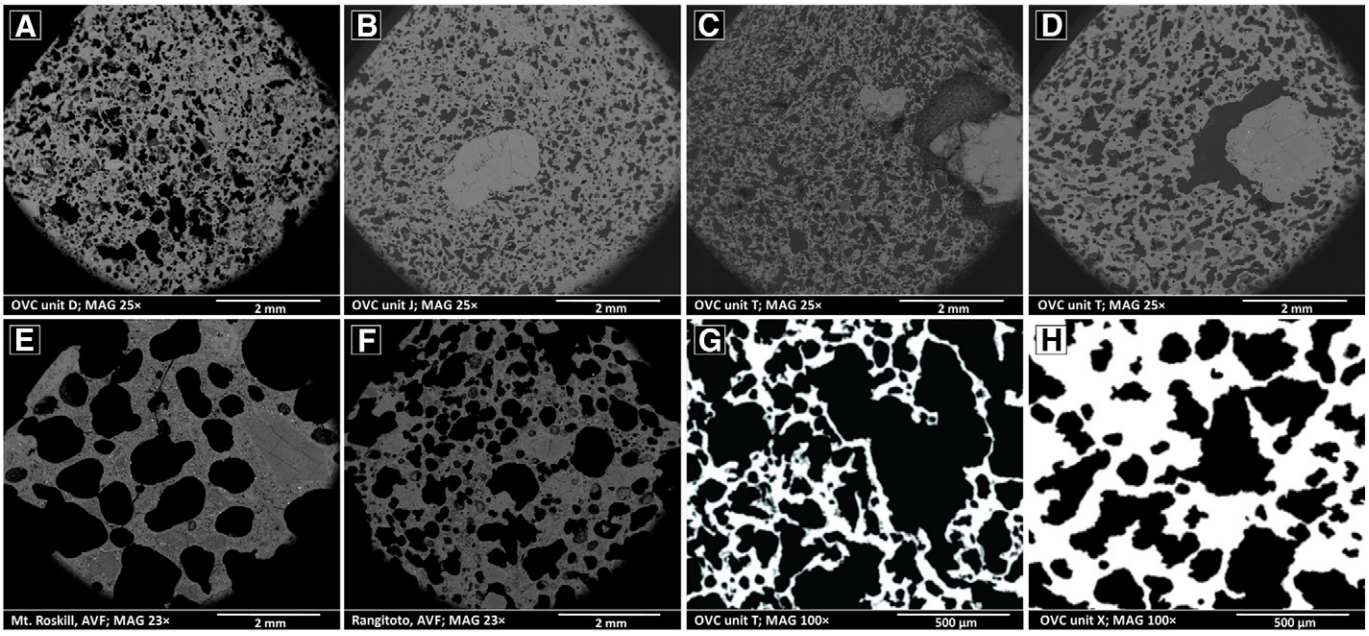

Fig. 7. SEM images of bombs/blocks (A–D, G, H) from OVC and SEM images of scoria fragments from Mt. Roskill (E) and Rangitoto (F), Auckland Volcanic Field (AVF) for comparison. The two samples from AVF exhibit a Hawaiian and Strombolian (or Violent Strombolian)-style eruptions (Kereszturi, unpublished data) as the vesicles show mostly spherical or subspherical shapes (Lautze and Houghton, 2007; Moitra et al., 2013). The textures of samples from OVC completely different from textures forming during these mild type of eruptions, however similar to Basaltic Plinian eruptions of Etna 122 BCE and Tarawera 1886 (Moitra et al., 2013).

with a bomb bed (unit X), which indicates that the two units did not form by explosions from a single vent. The fragmentation during stronger discrete eruptions produced a higher amount of fine ash deposited by wet pyroclastic surges and tephra fallout. The slightly higher proportion of accidental fragments that originate from the shallow laharic basement demonstrates that the eruption loci were still of shallow depths without notable excavation.

5.3. Bomb beds with ash (Bb_A)

5.3.1. Description

The Bb_A lithofacies is clast-supported and predominantly made up from mud-coated, weathered (oxidised at very proximal locations) and fresh juvenile lapilli and bomb sized fragments with various amounts of fines, usually without stratification (Fig. 4). The ratio of the ash and lapilli/bomb fragments can vary vertically within the same unit. In a few locations the ash rich portions are arranged into hardly distinguishable graduated sheets. The majority of coarse juvenile fragments are 3–10 cm in size with a maximum of 25–30 cm in diameter in loosely packed clast-supported beds. The bigger clasts sometimes display shapes generated by plastic deformation. Some of these flattened clasts have experienced agglutination. Other clasts are dense lapilli and blocks with fractured edges exhibiting various degrees of alteration. At the NW corner of the quarry the fragments are oxidised, but in other locations yellowish to brownish alteration of clasts can be observed. The ash componentry is identical to the other ash-rich units. Mud-coating is common to all clasts and at all grain size classes. Ballistic bomb sags are not visible, but the impact of the biggest andesitic boulders can form minor distortions. The thickness of the units can vary between 0.3 and 3.5 m.

5.3.2. Emplacement interpretation

The tephra associated with **Bb_A** units have most likely originated from two sources. The average grain size, the shape of the coarsest fragments, lack of matrix, and the dominance of moderate to highly vesiculated juvenile fragments suggest that these units have originated from Strombolian-style eruptions (McGetchin et al., 1974; Houghton and Hackett, 1984). The documented clast flattening and agglutination imply occasionally higher retained heat, which might have been caused by the fluctuation of the effusion rate during Strombolian activity. However the varying proportions of fine material, componentry (e.g. mud-coated fragments and aggregates), fractured, altered juvenile blocks and accidental boulders all suggest that fresh juveniles erupted through slurry-filled craters. The altered earlier fragments were mixed with Strombolian products. The adhering dust on the surface of clasts across a wide spectrum of grain sizes suggests a broad recycling and in-situ

Table 1
Bubble volume (BV), bubble number density (N_V) and typical sizes (equivalent diameter: EqDi) and shapes of vesicles (Regularity, Shape factor) for distinct units and clasts from the proximal sequence of EER.

Sample code	Density derived (BV) (%)	2D BV (%) (ImageJ)	2D BV (%) (Foams)	N_V (corr) (mm^{-3})	EqDi range (mm)	Mean EqDi (mm)	Mean Area (mm^2)	Regularity (Shea et al., 2010)	Shape factor (Orsi et al., 1992)
A1	46.6	42	26.5	1.22×10^3	0.015–5.168	0.112	0.034	0.8501	0.6023
D1	44.2	45.1	25.9	1.55×10^3	0.015–4.015	0.136	0.046	0.8302	0.5989
D3	43.3	43.8	31.6	2×10^3	0.012–7.116	0.166	0.114	0.831	0.6144
H2	38.3	47.7	28.8	1.57×10^3	0.005–3.939	0.172	0.061	0.8322	0.6066
H3	39.1	28.4	24.6	1.71×10^3	0.005–2.154	0.143	0.041	0.8807	0.6357
J4	39	31.2	25.5	3.15×10^3	0.005–2.076	0.097	0.025	0.8739	0.6045
T1	51.4	47.9	28.4	4.69×10^3	0.005–5.351	0.189	0.108	0.7948	0.5663
T3	44.5	53.3	28.9	1.7×10^3	0.005–14.895	0.308	0.397	0.8147	0.6050
X2	39.8	38.1	22.1	6.5×10^2	0.005–2.622	0.177	0.070	0.8333	0.5957
X3	26.4	44.1	27.2	1.46×10^3	0.006–1.341	0.172	0.036	0.848	0.4931

palagonitization of the glassy rinds of pyroclasts (Houghton and Smith, 1993). Strombolian/Hawaiian and phreatomagmatic eruptions represent usually very different type of magma fragmentation (Wohletz and McQueen, 1984), however, there are a few documented eruptions that exhibited both fragmentation process at the same time (Moore et al., 1966; Kienle et al., 1980; Dzurisin et al., 1995; Valentine et al., 2000). The Bb_A unit products did not form by magmatic fragmentation alone. The high portion of dust-adhered fragments demonstrates an abundance of water in the eruption plume. There are two alternative models for the magma fragmentation and mixture of tephra from two contrasting eruption styles. Depending on the variations of vent geometry and hydrological conditions the products could have originated from different parts of the same vent or fissure (Houghton and Schmincke, 1986; Dzurisin et al., 1995) or from two or more localized vents along a fissure (Kienle et al., 1980; Pedrazzi et al., 2014a; Belousov et al., 2015).

5.4. Spatter-scoria bomb beds (Bb)

5.4.1. Description

Spatter-scoria bomb beds are clast-supported without any internal bedding. The upper boundary is sharp, but the lower can be sharp or interfingering with Ab_C-type units. **Bb** units are made up from oxidised or fresh juvenile fragments of plastically deformed and cauliflower-shaped coarse lapilli and blocks or bombs with minor amounts of medium lapilli (0.5–1 cm in size). The grain size distribution of these beds implies better sorting than the other lithofacies. The average clast size ranges between 3 and 10 cm, the maximum clast size is observed up to 30 cm. These units often exhibit agglutination as well as locally confined welding (Fig. 4).

5.4.2. Emplacement interpretation

The lack of admixed ash, the plastically deformed fragments and the short dispersal range of the rapidly thinning beds suggest that **Bb** beds originated from vents characterized by low energy Strombolian and/or Hawaiian-style activity. However, the existence of the large number of dense cauliflower-shaped blocks suggests rapid cooling prior to eruptions (Kienle et al., 1980). In addition, the interfingering ash-dominated lithofacies (Ab, Ab_C) demonstrates that other phreatomagmatic vents could have been active at the same time referring to the abundance of water to other parts of the dyke.

6. Density and vesicle microtexture analysis

Clast densities and vesicle textures (e.g. vesicle size and shape, vesicle number densities) provide information on characterizing the conditions of magma ascent and degassing, and may also elucidate the changing conditions within the conduit between consecutive eruptive phases (Houghton and Wilson, 1989; Parfitt, 2004; Moitra et al., 2013). The skeletal (absolute) density determined for blocks/bombs was 2.85–2.90 g/cm^3. The bombs/blocks exhibit different envelope densities than the lapilli size clasts. The lapilli ($-3\ \phi$) average densities are between 1.27 and 1.33 g/cm^3, while the bombs have densities of 1.52–1.54 and 1.72–1.82 g/cm^3. The modes show a similar pattern of 1.0–1.2 g/cm^3 for lapilli size and 1.5–1.7 g/cm^3 for bomb/block size (Fig. 6). The 3D vesicularity was calculated applying a 2.85 g/cm^3 density, yielding values significantly higher (26.4–51.4%) than the FOAMS-calculated integrated 2D vesicularities (22.1–31.6%). The 2D shape of the bubbles usually exhibits irregularities (polylobate shapes) due to frequent coalescence inducing a large-scale interconnectivity of the vesicles (Fig. 7, Table 1). Most of the equivalent diameters of vesicles are smaller than 1 mm and range between 0.005 and 14.9 mm with an average of 0.97–0.308 mm. Typically, 50–70% of bubbles are smaller than 0.1 mm, except for unit X where these small bubbles made up only 16–20% (Table 1). Vesicle number density values vary from 6.5×10^2 to 4.69×10^3 mm^{-3} (Fig. 9, Table 1).

6.1. Interpretation of observed density and vesicle microtextures features

In comparison with the results of previous density measurements from OVC, similarities exist between our lapilli densities and the density measurements of clasts from "S beds" and "Pb beds" from Houghton and Hackett (1984). Minimum values are 1 g/cm^3, but our maximum values are larger by 0.5 g/cm^3 than earlier results. That could be an explanation, why our mean densities are larger at approx. 0.1 g/cm^3. The bomb/block densities of this study are similar to the bomb density values published in Houghton and Hackett (1984) from the unwelded parts of the inner scoria cone. The density differences between the two examined clast sizes suggest that they originated from different parts of the magma and may represent different fragmentation and eruption styles. Furthermore, units H and X are more heterogeneous with clasts also having higher densities. It is clear that the heterogeneous clast assemblage originated from the same eruption phase; hence any conduit process (e.g. intensified degassing from a more fluid melt) could have been responsible for the recorded density diversities.

Even the vesicle textures and shapes from the most Strombolian-like beds (Bb_A and Bb lithofacies) are completely different to textures originating from other Strombolian (violent Strombolian) and Hawaiian eruptions (Lautze and Houghton, 2007; Gurioli et al., 2008; Cimarelli et al., 2010; Stovall et al., 2011; Moitra et al., 2013; Kereszturi and Németh, 2016) (Fig. 7). Vesicle textures from the OVC exhibit similar features to the products of basaltic Plinian eruptions of Etna, 122 BCE and Tarawera, 1886 (Sable et al., 2006; Moitra et al., 2013) and the hydromagmatic eruptions of the Ilchulbong tuff cone (Murtagh et al.,

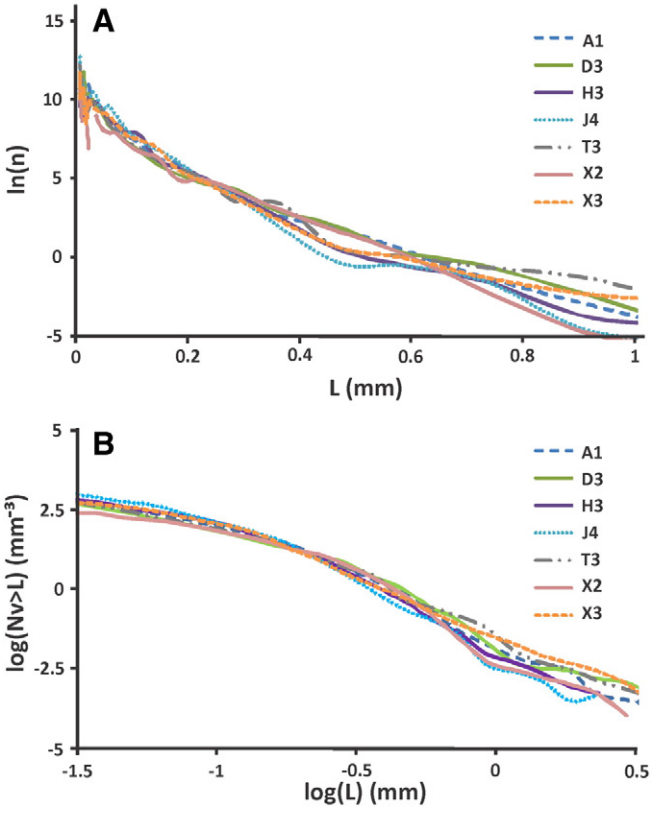

Fig. 8. A Vesicle size distributions (VSD) are ln(n) as a function of L plots, with ln(n) the log of the vesicle number densities per size class, and L is the equivalent diameter in mm. The left part of the segment mostly reflects multiple stages of bubble nucleation and growth. The lower part of the VSD slopes often exhibit coalescence (e.g. J4, T3) which may have occurred at multiple stages. B Cumulative vesicle size distributions (CVSD) are $\log(N_V > L)$ as a function of log(L) plots, where N_V is the total vesicle number density. Vesicle density measurements were used based on the objects per cubic mm greater than L. CVSD trends also suggest multiple stage of nucleation and growth with coalescence and bubble collapse events in most of the cases (e.g. A1, D3, J4, T3, X2) (Shea et al., 2010).

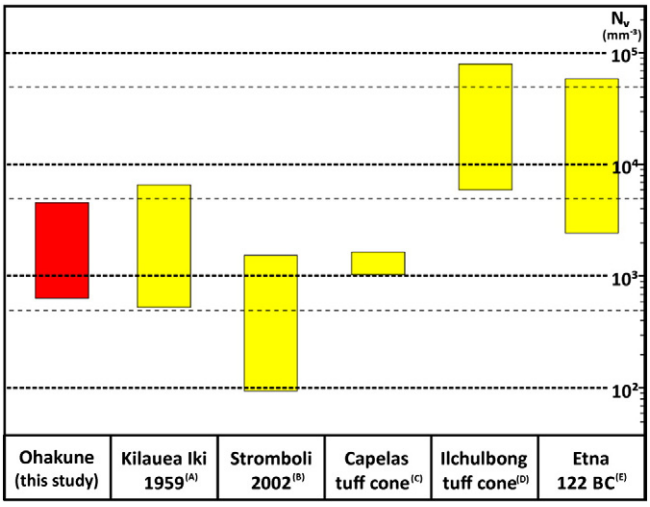

Fig. 9. Range of OVC bubble number density (N_V) values measured on blocks and bombs from Bb and Bb_A type units in comparison with selected eruptions exhibiting different eruption styles; (A) Stovall et al. (2011);(B) Lautze and Houghton (2007); (C) Mattsson (2010); (D) Murtagh et al. (2011); (E) Sable et al. (2006).

2011). Based on tephra properties of distal outcrops and the estimated dispersal it is assumed that the Ohakune eruption does not correspond to basaltic Plinian eruptions, thus it is proposed that the observed vesicle textures may have formed by effects of interaction with external water. Results of quantitative analysis of FOAMS verify coalescence of the vesicles and indicate multiple stages of nucleation and growth (Fig. 8). The calculated bubble number density values of the OVC eruption are lower than those from the Ilchulbong tuff cone, but within the range of other small-volume eruptions from Hawaiian and Taalian in style (Fig. 9) (Murtagh et al., 2011; Stovall et al., 2011).

7. Petrology, geochemistry and thermobarometry

The fresh block/bomb fragments of the Ohakune andesite are dark grey in colour with inequigranular/hyalopilitic textures, containing 0.1–0.8 cm light green to yellowish, mostly isometric or broken pyroxene and olivine crystals and crystal nodules (Fig. 10). Even the densest clasts have visible vesicles with uneven distributions. We determined the major element geochemistry of glass fragments from ash samples as well as of groundmass glass and phenocrysts of bomb/block fragments (Appendix 1). The main observation is that the blocks/bombs groundmass glass results display a restricted compositional range in comparison with ash fragments (Figs. 11–13). Harker diagrams of oxide distributions follow trends of depletion in MgO, FeO, and CaO, enrichment of K_2O, and Na_2O, and initial enrichment followed by depletion in Al_2O_3 and Na_2O versus SiO_2 (Fig. 11), although there is significant scatter in the low- to intermediate silica range. Glass compositions range from basaltic andesite to rhyolite in the TAS classification, i.e. range to much more evolved compositions than the bulk rock (57% SiO_2) (Hackett and Houghton, 1989). Strikingly, compositions broadly follow an iron enrichment trend in the AFM diagram (Fig. 12), atypical for continental arc volcanic products (e.g. Ruapehu compositions, Price et al., 2012) and more characteristic for magmas related to decompression induced melting.

We examined compositional variations through time by plotting chemical data from consecutive units (Fig. 13). The ash geochemistry exhibits a great compositional variation within all the examined oxides, and its average values show significant fluctuations through time (SiO_2: 62–67 w%; K_2O: 1.2–2.7 w%; MgO: 1.5–3.1 w%). In contrast, the averages of groundmass glass compositions measured from blocks/bombs display comparatively minor variations (Figs. 11 and 13).

Microscopic and SEM imaging indicates that the crystal cargo consists of olivine, clinopyroxene (cpx) and orthopyroxene (opx). The olivine crystals display corona-textured reaction rims due to dissolution followed by opx overgrowth (Zellmer et al., 2016) (Fig. 10). Furthermore, touching crystals of cpx and opx are in chemical equilibrium (Fig. 10), allowing the calculation of P-T conditions of crystallization (Table 2). The groundmass of the rock is usually moderately microlithic with plagioclase laths up to 50–60 μm in size and isometric opx, cpx and olivine microphenocrysts. The groundmass microlite content of the examined samples varies from 15 to 25%.

We calculated crystallization temperatures and depth by thermobarometry utilizing Putirka's (2008) two-pyroxene calibrations. Our results yield lower temperatures (1034–1053 °C) and pressures (4.8–5.4 kbar) than previous estimates based on cpx-liquid thermobarometry (Table 2) (Deering et al., 2011). Using 2.7 g/cm^3 for crustal density (Deering et al., 2011), the two-pyroxene method indicates 16–18 km crystallization depth (Table 2).

7.1. Evaluation of the results of petrology, geochemistry and thermobarometry

The observed iron enrichment trend suggests that magmatism at the OVC is related to decompression-melting with little contribution from the subducting slab. This is consistent with the location of the OVC at the southernmost end of the TVZ at the tip of the southwards propagating extension zone. Further, the relatively minor groundmass glass compositions measured from blocks/bombs suggest that the compositional characteristics of the eruptive products are not attributable to multiple magma batches with different chemical compositions. Instead, variations in ash compositions may reflect changes in magma ascent

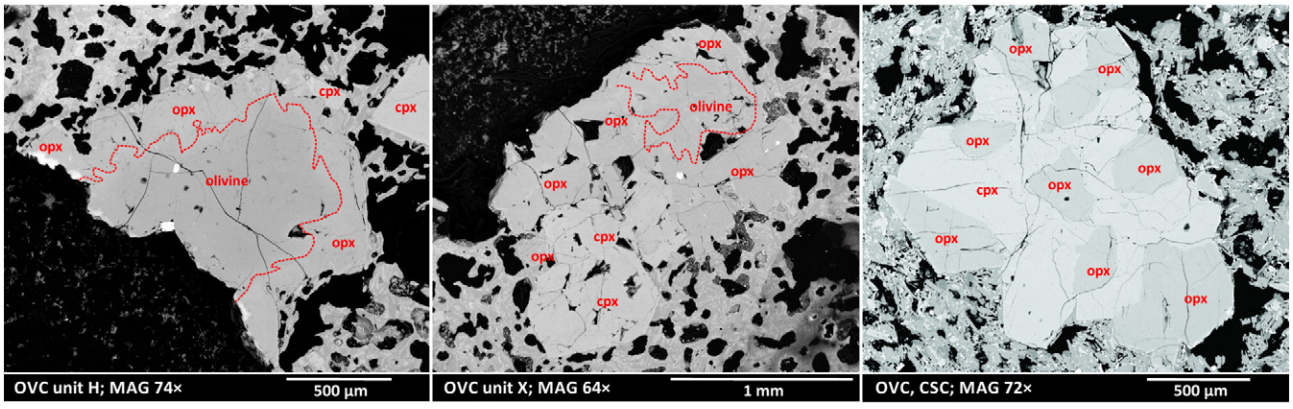

Fig. 10. SEM images of phenocrysts (antecrysts) from Bb and Bb_A type units showing the hyalopilitic textures and growth relationship between olivine, orthopyroxene and clinopyroxene. Element mapping was executed by EDAX.

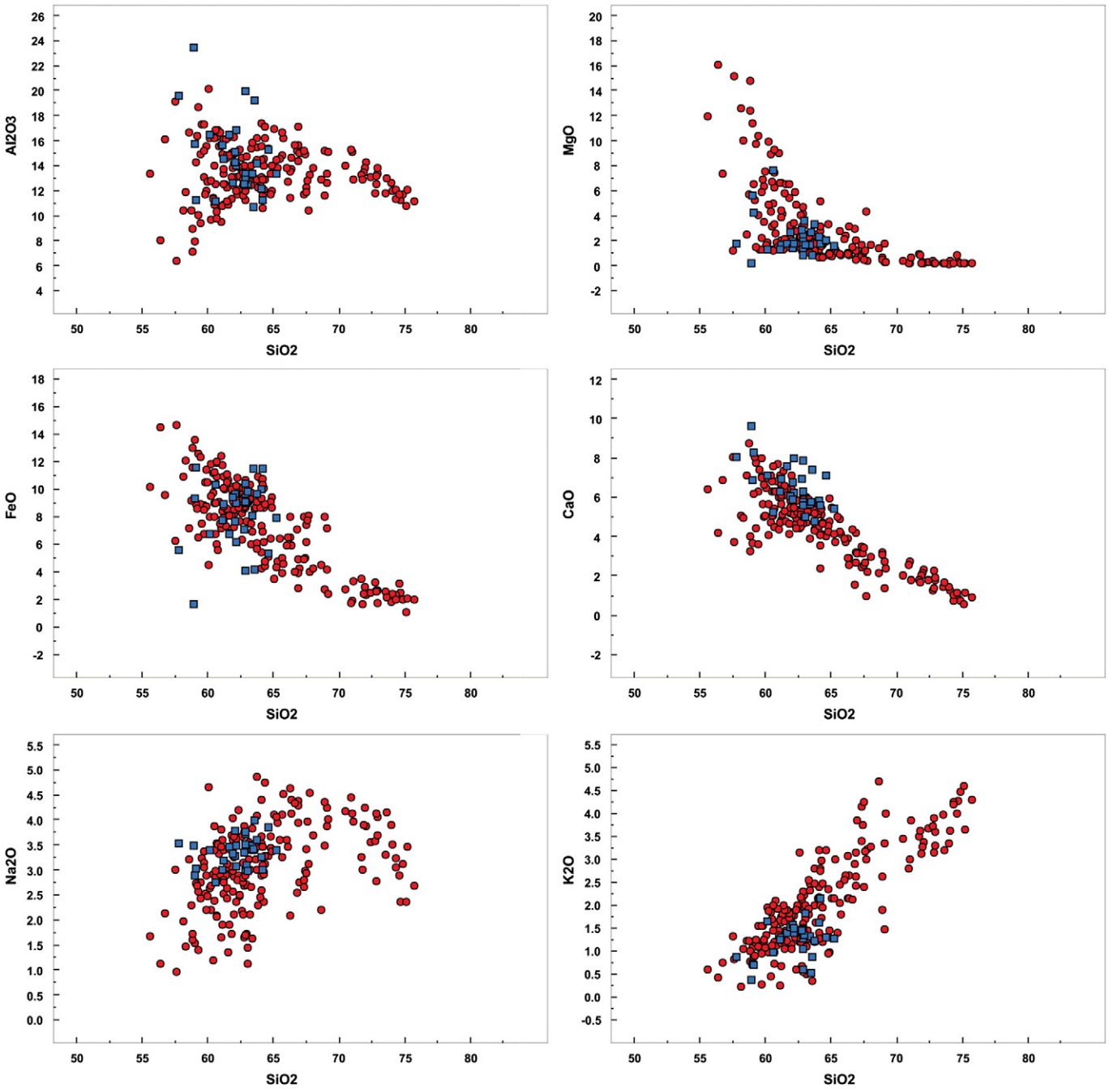

Fig. 11. Harker diagrams for selected major element oxides normalized to water-free compositions. Red circles represent ash fragment, blue rectangles represent groundmass glass compositions of blocks and bombs.

rate accompanied by variations in the degrees of cooling, degassing, decompression rates and resulting microlite crystallization (Cashman and Blundy, 2000). Turning to the phenocryst phases, the OVC andesitic magma may represent a mixture of crystals and melts as a result of polybaric fractional crystallization and magma mixing, similar to other erupted andesitic to dacitic rocks from Tongariro Volcanic Centre (Price et al., 2012). For example, the lack of plagioclase phenocrysts in these intermediate composition eruption products suggests that the nodules and phenocrysts of opx, cpx and olivine may represent antecrystic material picked up from a crystal mush of an earlier stalled and cooled magma (e.g. Zellmer et al., 2014). One possible petrogenetic scenario is that this crystal mush is remobilized by intrusion of andesitic to dacitic melt, which ultimately carries the earlier formed crystals of olivine, opx, and cpx to the surface. Corona textures of the olivines may have formed during mush remobilization at depth. The final crystallization event occurred at shallow (tens to hundreds of meters) depth, forming the microlitic groundmass during the relatively fast magma ascent at the onset of eruption. The calculated crystallization depths are slightly shallower than the previous calculations by Deering et al. (2011) (Table 2) yet both results are within the acceptable depth range of a crystal mush zone or magma source.

8. Eruptive volume calculations

The eruptive volumes are essential for understanding the evolution, eruptive styles and related hazards of small-volume volcanoes (Guilbaud et al., 2012; Le Corvec et al., 2013; Kereszturi et al., 2014; Bebbington, 2015; Németh and Kereszturi, 2015). Monogenetic

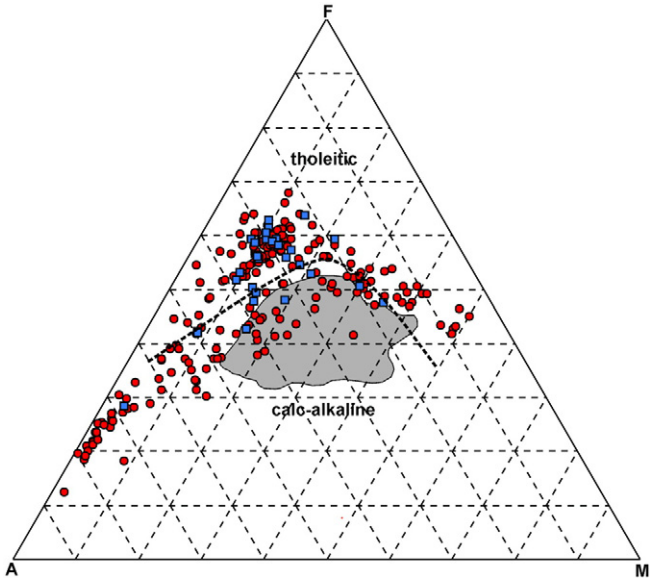

Fig. 12. AFM diagram shows glass compositions measured on ash fragments (red circles) and groundmass glass of blocks and bombs (blue rectangles) in comparison with whole rock compositions of Ruapehu volcano (grey field) (Price et al., 2012, e-appendix 10).

volcanoes usually have a wide variety of eruptive styles and products as demonstrated by the volcanic sequence of the OVC. To account for this complexity, we employed the eruptive volume scheme used in the Auckland Volcanic Field, New Zealand (Kereszturi et al., 2013). Due to the overall small proportion of lithics in the exposed sequences, we do not expect diatreme structures beneath the edifice, thus we calculate volumes for proximal ejecta rings and scoria cones as well as distal tephra deposits (Fig. 14). The edifice volume was calculated from a DTM using uniformly 585 m asl plane as the pre-eruptive surface, whereas the distal tephra volume was calculated by applying exponential thinning (Pyle, 1989) with the considerations of thinning trends measured within the quarry and thickness and sedimentological observations at distal outcrops. Using our componentry, density, and vesicularity data (Fig. 6, Table 1) and the earlier density measurement for the central scoria cone (Houghton and Hackett, 1984), we could convert bulk distal tephra and edifice volumes to DRE volumes (Fig. 14, Table 3), using the method developed by Kereszturi et al. (2013).

The obtained 12.36×10^6 m^3 DRE total erupted volume includes 2.99×10^6 m^3 (24.2%) rough DRE distal volume and 9.36×10^6 m^3 (75.8%) edifice DRE volume. It seems that the DRE volume of the phreatomagmatic and magmatic products is broadly equal, but scoriaceous deposits are dominant within the edifices (Fig. 4). Due to the morphological differences between the west ejecta ring (WER) and east ejecta ring (EER) (Fig. 2) we calculate the volume of the WER edifice only with phreatomagmatic successions. Uncertainties exist surrounding the possible volumes of eroded sequences of the eastern part of the volcanic complex. The calculated distal volume should be considered only as a minimum value due to the small number of distal thickness measurement. The accuracy of topographic data and data availability for pre-eruptive surface determination can also contribute to the uncertainties associated with volume calculations.

9. Discussion

9.1. Fragmentation and eruptive styles

Despite the absence of accretionary lapilli and the rare occurrence of blocky glass fragments, other features of pyroclastic fragments (e.g. glass alteration – palagonitization, aggregates of ash, presence of mud-coating and secondary minerals inside the cavities) is indicative of a hydrovolcanic origin of the ash-rich beds (as evidenced by Ab and Ab$_C$ lithofacies) (Sheridan and Wohletz, 1983; Cioni et al., 1992). Furthermore, sedimentary features such as plastically deformed bomb sags and soft sediment deformations support a water-saturated nature of pyroclastic density currents (Fisher and Schmincke, 1984; Németh et al., 2001). At first glance, the coarser bomb beds (Bb$_A$ and Bb lithofacies) of the ejecta rings show a magmatic (likely Strombolian) origin through their grain size properties (coarse fragments with better sorting) and plastically deformed shapes. However these beds commonly contain cauliflower-shaped bombs (Fig. 4), which are usually characteristic of hydrovolcanic fragmentation (Kienle et al., 1980; Fisher and

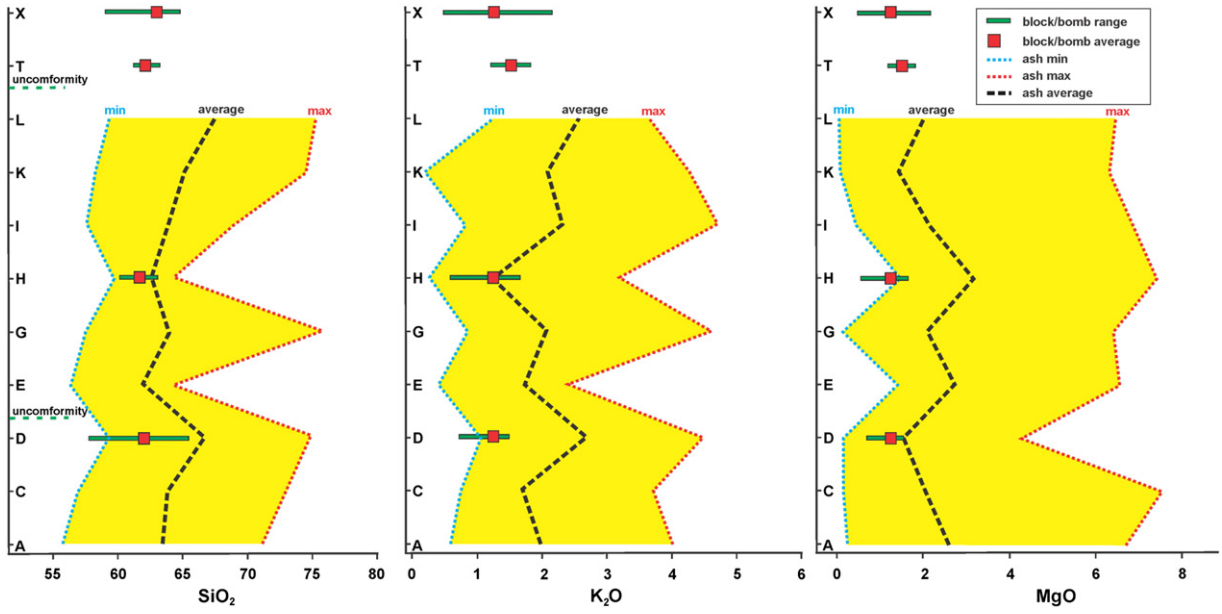

Fig. 13. Compositional variations of SiO_2, K_2O and MgO of ash (yellow fields) and blocks and bombs through the sequence.

Table 2
Results of geothermobarometry calculations utilizing Putirka's (2008) two-pyroxenes calculations on phenocrysts of bombs and blocks. Earlier calculations (Deering et al., 2011) indicate deeper source region for the erupted magma.

Two-pyroxenes geothermobarometry, sampled units	Eqn 36	Eqn 37	Eqn 38	Observed	Estimated depth (km)
	T (°C)	T (°C)	P (kbar)	K_D (Fe–Mg)	
D	1046	1034	5.4	0.981	18
D	1041	1052	4.8	0.850	16
H	1035	1053	5.3	0.970	17.8
X	1043	1036	4.8	0.847	16
Cpx-liquid geothermobarometry (Deering et al., 2011)	Eqn 33	Eqn 34	Eqn 31	Eqn 35	Calculated depth (km)
	T (°C)	T (°C)	P (kbar)	K_D (Fe–Mg)	
Ohakune	1137	1152	6.4	0.281	21.4

Schmincke, 1984). Moreover the ash fragments of the Bb_A beds show identical features with fragments from the ash beds. The examined vesicle microtexture properties of the largest clasts from the Strombolian beds do not exhibit the typical micro-textural characteristics of Strombolian fragments (Fig. 7). The size and shape of vesicles as well as the bubble number density values might reflect an increased degree of cooling and higher viscosities similar to the properties of hydrovolcanic eruptions. It seems that throughout the course of the activity water was abundant, which implies the eruptions were unable to permanently dry out the shallow basement (Lorenz, 1986; Lorenz, 2007). The componentry analyses exhibit small percentages of accidental fragments dominantly from the subsurface laharic deposits, indicating that excavation was minor and the fragmentation likely occurred at very shallow depth. The detected heterogeneities of clast densities in units H and X indicate mingling of degassed dense magma with hotter gas-rich melt within the conduit. This suggests that the ascent rate extensively fluctuated and the stalling degassed upper part was broken through from time to time by fresh magma with varying intensity (Lautze and Houghton, 2007). The higher ascent rates of fresh magma resulted in sustained Strombolian, occasionally Hawaiian eruptions with little influence from water (water/magma ratio around 0.1), while the lower ascent rates dominantly led

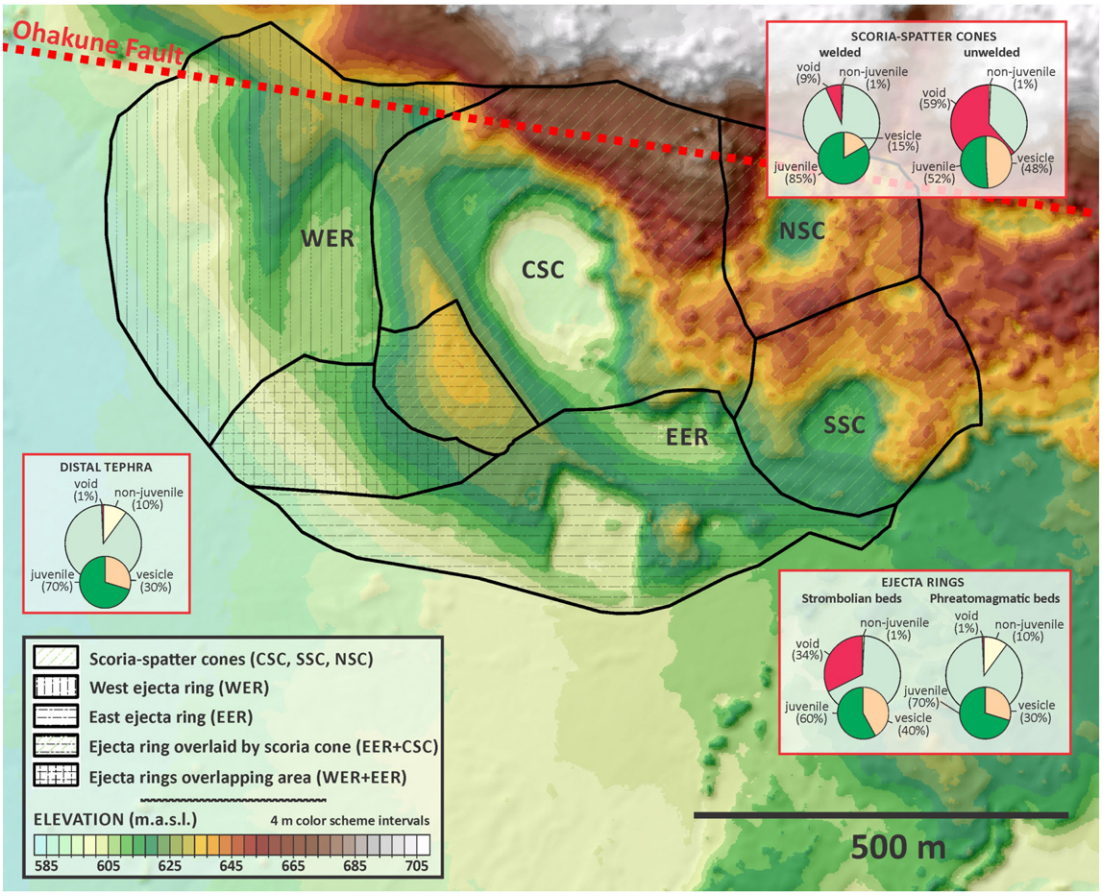

Fig. 14. Delineation of distinct edifices of OVC. The obtained area and thickness values were applied for bulk volume calculations. Pie charts represent the DRE correction scheme applied for volume estimation from the different parts of the volcanic complex (Kereszturi et al., 2013). As the first step of the DRE corrections, the pie bigger charts imply the proportion of juvenile, non-juvenile and interparticle void space. Secondly, the smaller pie charts show the remaining juvenile content was corrected with the available vesicularities.

Table 3
Results of DRE volume estimations for the OVC based on bulk edifice volume calculated from DTM of Ohakune and DRE correction schemes presented at Fig. 14.

	Bulk volume (10^6 m^3)	DRE index	DRE volume (10^6 m^3)
Central scoria cone (CSC)	8.07	0.487	3.98
South scoria cone (SSC)	3.51	0.208	0.73
North scoria cone (NSC)	3.34	0.208	0.69
West ejecta ring (WER)	3.99	0.45	1.80
East ejecta ring (EER) (Total)	5.12		2.16
EER (magmatic)	2.38	0.39	0.93
EER (phreatomagmatic)	2.74	0.45	1.23
Total Edifice	24.03		9.36
Distal	4.80	0.623	2.99
Total	28.83		12.36
Total magmatic	17.30		6.34
Total phreatomagmatic	11.53		6.02

to phreatomagmatic eruptions with higher water concentrations. The transitions from phreatomagmatic to Strombolian eruptions and vice versa were rapid.

9.2. Eruption history

Although the initial craters are highly obscured, the geomorphology, calculated volume and stratigraphy is inconclusive for the existence of a kilometre wide tuff ring (Houghton and Hackett, 1984). In contrast, we envisage an elongated composite ejecta ring around an at least 600 m long eruptive fissure aligned to the Ohakune Fault, similar to several examples such as Izu-Oshima, Japan (Sumner, 1998); Hverfjall eruptive fissure, Iceland (Mattsson and Höskuldsson, 2011); Easy Chair, Lunar Crater Volcanic Field, USA (Valentine and Cortés, 2013); and Tolbachik, Russia (Belousov et al., 2015). The eruptive centre was initiated by hydrovolcanic eruptions characterized by a sustained low eruptive column due to the abundance of surface and groundwater. The resulting ejecta ring was 15–20 m high, 300–400 m wide along the fissure and characterized by dominantly debris jets and fallout deposits interbedded by layers related to wet pyroclastic density currents (Figs. 4 and 15). The subsequent eruptions were localized into widened and disjointed vents usually inducing changes in mass flux within other areas of the vent zone (Valentine and Gregg, 2008). The usual fluctuating pressure conditions and ascent rates (Keating et al., 2008) and the result of alternations of magmatic and phreatomagmatic eruptions which may have been facilitated through the increased entry of groundwater into the shallow plumbing system. This, and increasing load on the crater rims could have easily led to the destabilisation of the loose surface deposits and the solidifying dyke margins as well (Gutmann, 2002) as demonstrated by the crater rim subsidence (syn-eruptive faulting) at the quarry (Fig. 4). The OVC sequence exhibits the relocation of the active vent(s) within the fissure zone (Fig. 4) probably due to the collapse of destabilized areas from time to time. The proximity of the source is clearly implied by the thermal oxidation along the fault (Fig. 4) similarly to the welded and agglutinated units of the CSC (Fig. 3). The frequent vent-shifting prevented the long term development of a single edifice. Rather, the products were accumulated at the southern margin of the fissure, forming a multisource ejecta ring structure (EER). This was constructed from water-influenced Strombolian bomb beds (Bb, Bb_A lithofacies) alternating with dense and wet pyroclastic surge and fallout deposits (Ab lithofacies). The deposited pyroclasts within the fissure zone were

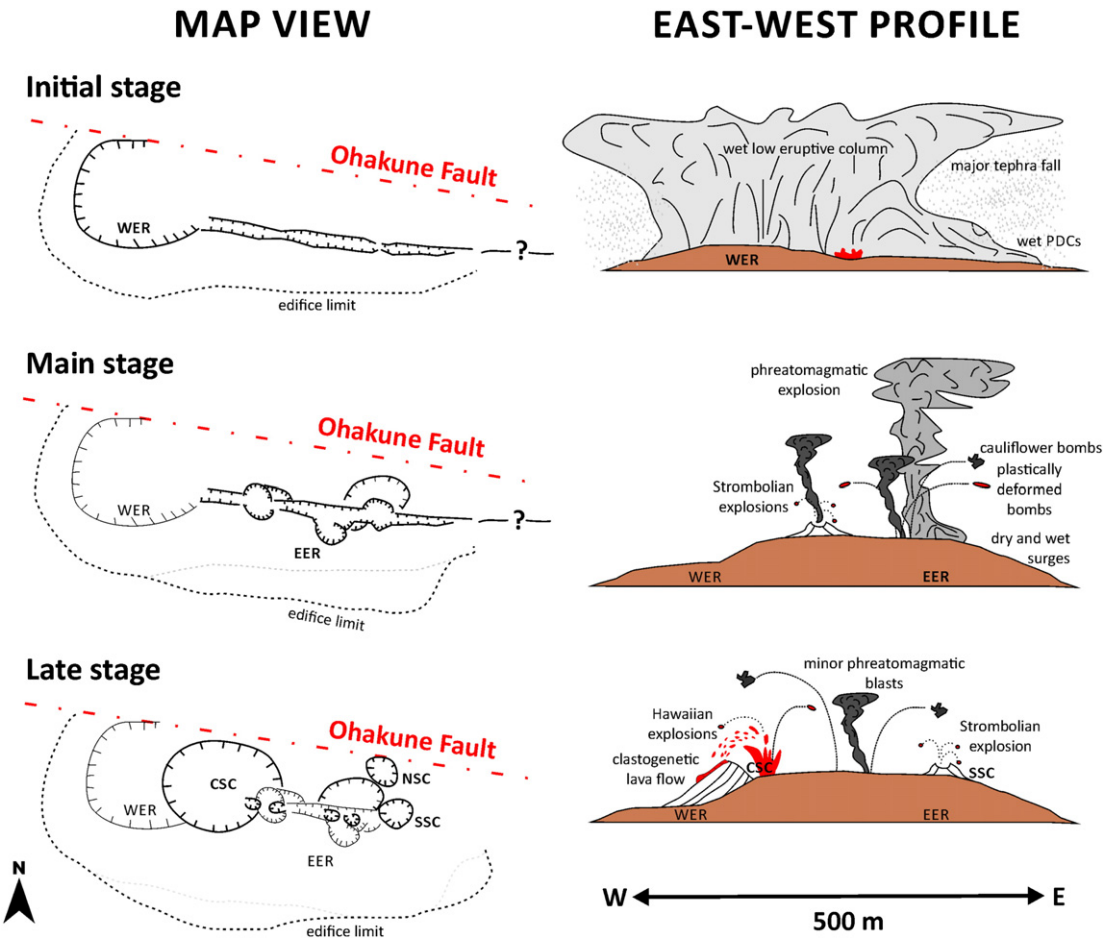

Fig. 15. Cartoon showing the evolution of facies architecture and eruptive mechanism during the OVC formation (see text for explanation).

removed by subsequent eruptions leaving a hollow, the smaller pits indicating the area where the dyke intersected the surface (Fig. 14). Similar morphological features have been reported from many monogenetic volcanoes within the Auckland Volcanic Field, such as Crater Hill (Houghton et al., 1999) and Three Kings (Kereszturi et al., 2014). Because the eastern part of the volcanic complex was eroded by the Mangawhero River, it is difficult to determine if there were any eruptions (possibly small phreatomagmatic blasts) along the eastern extension of the fissure. The late stage evolution was characterized by localization of stable vents producing Strombolian/Hawaiian fountains due to higher ascent rates and decreased water influence, however the axis of the fissure remained unburied indicating the existence of vent-clearing phreatomagmatic blasts along the other part of the fissure (Fig. 15).

9.3. Volcanic hazard assessment

The eruptive styles associated with small-volume volcanoes are usually strongly influenced by magma ascent rates (Wilson and Head, 1981; Parfitt, 2004; Valentine and Gregg, 2008) and the availability of external water (Kokelaar, 1986). Despite the lack of direct observations of magma ascent rates, there are various methods for its estimation such as field observations of facies architectures (Houghton et al., 1999), average size of mantle xenoliths (Sparks et al., 1977) and water-content and zonation of olivine crystals (Peslier and Luhr, 2006; Jankovics et al., 2013). The Ohakune sequence exhibits transitions between phreatomagmatic and Strombolian as well as Strombolian and Hawaiian eruptive styles, the latter implying ascent rates varying around 0.1 m/s (Parfitt, 2004) in the case of a point source stabilized vent. The earlier stage fissure or multiple source eruptions could have been characterized by fluctuating high ascent rates coincident with significant water influx and increased water/magma ratios. Near surface ascent rates might have exhibited differences to the lower feeding systems due to guidance of the fault and syn-intrusive extension. We assume an 1 m width for the feeder dyke as an average of observations (Geshi et al., 2010), and note that the facies architecture (Houghton et al., 1999) and possible effects of fault guidance suggest a similar or shorter dyke length for the lower feeding system. Combining, the possible source depth estimated of 18 km obtained by two-pyroxene geothermobarometry with an average ascent rate of approx. 0.1 m/s, we argue that the magma may have reached the surface within 50 h. Considering the range of ascent rates for the shallow plumbing system (0.01–1 m/s), and the extent of the active vent area, it is possible to calculate effusion rates. This analyses suggests peak effusion rates of 25 m^3/s for the initial hydrovolcanic phase, 8 m^3/s for the late stage Hawaiian fountains and <0.1 m^3/s for the lowest discharge periods. Using the volume calculations and ascent/effusion rates it is possible to estimate the duration of the activity of the OVC. The duration using an inferred discharge rate of 1–2 m^3/s corresponds to a maximum duration of 2.5 to 5 months for the entire event. Even though this duration seems to be rather long for this type of volcanism however the lack of erosional structures throughout the eruptive sequence would suggest a shorter duration. In addition, the OVC erupted from multiple vents, the timing and duration of each vent remains unclear due to scarce outcrops to examine stratigraphic relationships and geochemical characteristics. It is also unclear whether each vent operated simultaneously or were there time gaps between such activities. These features of the OVC have to be studied in more detail in the future.

It is difficult to evaluate if there is any relationship between the OVC's feeding system and the main conduits of Ruapehu volcano, because the deep structure of southern slope and ringplain of Ruapehu volcano is not known. Magnetotelluric surveys did not propose large scale accumulation of magma shallower than 14 km beneath Ruapehu (Ingham et al., 2009). However, the plumbing system might include the network of small-volume dispersed magma storages in the mid- and shallow crust (Price et al., 2012). Our proposed 16–18 km depth for the accumulation of magma erupted at OVC corresponds to the upper part of mush zones of the heavily intruded lower crust (Deering et al., 2011). In spite of the analogous petrogenesis of the OVC and some of Ruapehu magmas (Price et al., 2012) we do not expect the OVC to have a closer relationship with the plumbing system of main conduit of Ruapehu than to any of the other three composite volcanoes of the Tongariro Volcanic Centre (Fig. 12). On the basis of the available major element oxide data, it appears that the eruptions around Ohakune represent the first precursors of the southward expansion of the andesitic arc of the TVZ, and that the OVC conduit is independent of the main feeder system of Mt. Ruapehu.

10. Conclusion

The OVC provides an opportunity to examine an eruptive sequence characterized by alternating eruptive styles. The resulting deposits indicate that the rising magma erupted through multiple vents by fire-fountaining to water-influenced Strombolian explosions alternated with phreatomagmatic blasts. It appears that after the initial vent opening, the most significant controlling factors were the changing vent geometries and variable interaction with external water, while the final phase was characterized by higher effusion rates, which enabled the isolation from the source of external water inducing fire-fountaining eruptions and the generation of short clastogenetic lava flows. This study has revealed that the volcanic architecture of the OVC is much more complex than previously believed, and that the phreatomagmatism was constantly present during its activity. This study indicates that the active vents can be unstable and abrupt changes in eruption location (likely influenced by faults) and eruption styles can occur, significantly increasing the hazard of such small-volume eruptions. The duration of several months of such events is also significant in terms of volcanic hazards and considerably longer than previously considered at OVC. It is believed, there is a very small likelihood of a future volcanic event in the same location yet for future similar eruptions in the southern TVZ (south of Ruapehu) they would have a similar duration under the same tectonic influences. The eruptive behaviour of the OVC is also considered typical for future monogenetic eruptions within the other parts of Taupo Volcanic Zone.

Supplementary data to this article can be found online at http://dx.doi.org/10.1016/j.jvolgeores.2016.07.005.

Acknowledgements

This research is supported by a Doctoral Scholarship of Institute of Agriculture and Environment, Massey University awarded to Szabolcs Kósik. We thank Lisa Diane Hicks for access to her land, and Tony Te Hore Taura and Robert Grossart for access to the Ohakune quarry. We are grateful to Andrew Steffert and Horizons Regional Council, Palmerston North, New Zealand for made available their LiDAR DEM. The authors highly appreciate the time and effort of journal reviewers Gerardo Carrasco-Núñez and Dario Pedrazzi for their comments to improve this manuscript.

References

Abrams, M.J., Siebe, C., 1994. Cerro Xalapaxco: an unusual tuff cone with multiple explosion craters, in central Mexico (Puebla). J. Volcanol. Geotherm. Res. 63 (3–4), 183–199.

Agustin-Flores, J., Németh, K., Cronin, S.J., Lindsay, J.M., Kereszturi, G., Brand, B.D., Smith, I.E.M., 2014. Phreatomagmatic eruptions through unconsolidated coastal plain sequences, Maungataketake, Auckland Volcanic Field (New Zealand). J. Volcanol. Geotherm. Res. 276, 46–63.

Agustín-Flores, J., Németh, K., Cronin, S.J., Lindsay, J.M., Kereszturi, G., 2015. Shallow-seated explosions in the construction of the Motukorea tuff ring (Auckland, New Zealand): evidence from lithic and sedimentary characteristics. J. Volcanol. Geotherm. Res. 304, 272–286.

Auer, A., Martin, U., Németh, K., 2007. The Fekete-hegy (Balaton Highland Hungary) "soft-substrate" and "hard-substrate" maar volcanoes in an aligned volcanic complex - implications for vent geometry, subsurface stratigraphy and the palaeoenvironmental setting. J. Volcanol. Geotherm. Res. 159 (1–3), 225–245.

Bebbington, M.S., 2015. Spatio-volumetric hazard estimation in the Auckland volcanic field. Bull. Volcanol. 77 (5), 1–15.

Belousov, A., Belousova, M., Edwards, B., Volynets, A., Melnikov, D., 2015. Overview of the precursors and dynamics of the 2012–13 basaltic fissure eruption of Tolbachik Volcano, Kamchatka, Russia. J. Volcanol. Geotherm. Res. 299, 19–34.
Blott, S.J., Pye, K., 2001. GRADISTAT: a grain size distribution and statistics package for the analysis of unconsolidated sediments. Earth Surf. Process. Landf. 26 (11), 1237–1248.
Büttner, R., Dellino, P., La Volpe, L., Lorenz, V., Zimanowski, B., 2002. Thermohydraulic explosions in phreatomagmatic eruptions as evidenced by the comparison between pyroclasts and products from Molten Fuel Coolant Interaction experiments. J. Geophys. Res. Solid Earth (1978–2012) 107 (B11) (ECV 5-1-ECV 5-14).
Cameron, E., Gamble, J., Price, R., Smith, I., McIntosh, W., Gardner, M., 2010. The petrology, geochronology and geochemistry of Hauhungatahi volcano, SW Taupo Volcanic Zone. J. Volcanol. Geotherm. Res. 190 (1–2), 179–191.
Capaccioni, B., Cuccoli, F., 2005. Spatter and welded air fall deposits generated by fire-fountaining eruptions: cooling of pyroclasts during transport and deposition. J. Volcanol. Geotherm. Res. 145 (3), 263–280.
Carrasco-Núñez, G., Ort, M.H., Romero, C., 2007. Evolution and hydrological conditions of a maar volcano (Atexcac crater, Eastern Mexico). J. Volcanol. Geotherm. Res. 159 (1), 179–197.
Cashman, K., Blundy, J., 2000. Degassing and crystallization of ascending andesite and dacite. Philos. Trans. R. Soc. Lond. A Math. Phys. Eng. Sci. 358 (1770), 1487–1513.
Cimarelli, C., Di Traglia, F., Taddeucci, J., 2010. Basaltic scoria textures from a zoned conduit as precursors to violent Strombolian activity. Geology 38 (5), 439–442.
Cioni, R., Sbrana, A., Vecci, R., 1992. Morphologic features of juvenile pyroclasts from magmatic and phreatomagmatic deposits of Vesuvius. J. Volcanol. Geotherm. Res. 51 (1), 61–78.
Cole, J.W., Graham, I.J., Hackett, W.R., Houghton, B.F., 1986. Volcanology and petrology of the Quaternary composite volcanoes of Tongariro volcanic centre, Taupo volcanic zone, Late Cenozoic Volcanism in New Zealand. R. Soc. N. Z. Bull. 23, 224–250.
Cronin, S.J., Neall, V., Lecointre, J., Hedley, M., Loganathan, P., 2003. Environmental hazards of fluoride in volcanic ash: a case study from Ruapehu volcano, New Zealand. J. Volcanol. Geotherm. Res. 121 (3), 271–291.
Deering, C., Bachmann, O., Dufek, J., Gravley, D., 2011. Rift-related transition from andesite to rhyolite volcanism in the Taupo Volcanic Zone (New Zealand) controlled by crystal–melt dynamics in mush zones with variable mineral assemblages. J. Petrol. 52 (11), 2243–2263.
D'Oriano, C., Bertagnini, A., Cioni, R., Pompilio, M., 2014. Identifying recycled ash in basaltic eruptions. Sci. Rep. 4.
Dzurisin, D., Lockwood, J.P., Casadevall, T.J., Rubin, M., 1995. The Uwekahuna Ash Member of the Puna Basalt: product of violent phreatomagmatic eruptions at Kilauea volcano, Hawaii, between 2800 and 2100 14C years ago. J. Volcanol. Geotherm. Res. 66 (1), 163–184.
Fisher, R.V., Schmincke, H.-U., 1984. Pyroclastic Rocks. Springer, Berlin.
Folk, R.L., Ward, W.C., 1957. Brazos River bar: a study in the significance of grain size parameters. J. Sediment. Res. 27 (1).
Froggatt, P.C., Lowe, D.J., 1990. A review of late Quaternary silicic and some other tephra formations from New Zealand: their stratigraphy, nomenclature, distribution, volume, and age. N. Z. J. Geol. Geophys. 33 (1), 89–109.
Geshi, N., Kusumoto, S., Gudmundsson, A., 2010. Geometric difference between non-feeder and feeder dikes. Geology 38 (3), 195–198.
Gómez-Vasconcelos, M.G., Villamor, P., Cronin, S.J., Procter, J., Kereszturi, G., Palmer, A., Townsend, D., Leonard, G., Berryman, K., Ashraf, S., 2016. Earthquake history at the eastern boundary of the South Taupo Volcanic Zone, New Zealand. N. Z. J. Geol. Geophys. 1–22.
Graettinger, A.H., Manville, V., Briggs, R.M., 2010. Depositional record of historic lahars in the upper Whangaehu Valley, Mt. Ruapehu, New Zealand: implications for trigger mechanisms, flow dynamics and lahar hazards. Bull. Volcanol. 72 (3), 279–296.
Graettinger, A.H., Valentine, G.A., Sonder, I., Ross, P.S., White, J.D.L., 2015. Facies distribution of ejecta in analog tephra rings from experiments with single and multiple subsurface explosions. Bull. Volcanol. 77 (8).
Guilbaud, M.-N., Siebe, C., Layer, P., Salinas, S., 2012. Reconstruction of the volcanic history of the Tacámbaro-Puruarán area (Michoacán, México) reveals high frequency of Holocene monogenetic eruptions. Bull. Volcanol. 74 (5), 1187–1211.
Gurioli, L., Harris, A.J.L., Houghton, B.F., Polacci, M., Ripepe, M., 2008. Textural and geophysical characterization of explosive basaltic activity at Villarrica volcano. J. Geophys. Res. Solid Earth 113 (B8).
Gutmann, J.T., 2002. Strombolian and effusive activity as precursors to phreatomagmatism: eruptive sequence at maars of the Pinacate volcanic field, Sonora, Mexico. J. Volcanol. Geotherm. Res. 113 (1), 345–356.
Hackett, W.R., Houghton, B.F., 1989. A facies model for a Quaternary andesitic composite volcano: Ruapehu, New Zealand. Bull. Volcanol. 51 (1), 51–68.
Head, J.W., Wilson, L., 1989. Basaltic pyroclastic eruptions: influence of gas-release patterns and volume fluxes on fountain structure, and the formation of cinder cones, spatter cones, rootless flows, lava ponds and lava flows. J. Volcanol. Geotherm. Res. 37 (3–4), 261–271.
Heiken, G., Wohletz, K., 1985. Volcanic Ash. University of California Press, Berkeley.
Horizons Regional Council, 2016. Elevation Model Supplied by Horizons Regional Council, New Zealand.
Houghton, B.F., Gonnermann, H.M., 2008. Basaltic explosive volcanism: constraints from deposits and models. Chem. Erde Geochem. 68 (2), 117–140.
Houghton, B.F., Hackett, W.R., 1984. Strombolian and phreatomagmatic deposits of Ohakune Craters, Ruapehu, New Zealand: a complex interaction between external water and rising basaltic magma. J. Volcanol. Geotherm. Res. 21 (3–4), 207–231.
Houghton, B.F., Nairn, I.A., 1991. The 1976–1982 Strombolian and phreatomagmatic eruptions of White Island, New Zealand: eruptive and depositional mechanisms at a "wet" volcano. Bull. Volcanol. 54 (1), 25–49.
Houghton, B.F., Schmincke, H.-U., 1986. Mixed deposits of simultaneous Strombolian and phreatomagmatic volcanism: Rothenberg volcano, East Eifel volcanic field. J. Volcanol. Geotherm. Res. 30 (1), 117–130.
Houghton, B.F., Schmincke, H.U., 1989. Rothenberg scoria cone, East Eifel: a complex Strombolian and phreatomagmatic volcano. Bull. Volcanol. 52 (1), 28–48.
Houghton, B.F., Smith, R.T., 1993. Recycling of magmatic clasts during explosive eruptions - estimating the true juvenile content of phreatomagmatic volcanic deposits. Bull. Volcanol. 55 (6), 414–420.
Houghton, B.F., Wilson, C.J.N., 1989. A vesicularity index for pyroclastic deposits. Bull. Volcanol. 51 (6), 451–462.
Houghton, B.F., Wilson, C.J.N., Smith, I.E.M., 1999. Shallow-seated controls on styles of explosive basaltic volcanism: a case study from New Zealand. J. Volcanol. Geotherm. Res. 91 (1), 97–120.
Ingham, M., Bibby, H., Heise, W., Jones, K., Cairns, P., Dravitzki, S., Bennie, S., Caldwell, T., Ogawa, Y., 2009. A magnetotelluric study of Mount Ruapehu volcano, New Zealand. Geophys. J. Int. 179 (2), 887–904.
Jankovics, M.É., Dobosi, G., Embey-Isztin, A., Kiss, B., Sági, T., Harangi, S., Ntaflos, T., 2013. Origin and ascent history of unusually crystal-rich alkaline basaltic magmas from the western Pannonian Basin. Bull. Volcanol. 75 (9), 1–23.
Keating, G.N., Valentine, G.A., Krier, D.J., Perry, F.V., 2008. Shallow plumbing systems for small-volume basaltic volcanoes. Bull. Volcanol. 70 (5), 563–582.
Kereszturi G. unpublished data.
Kereszturi, G., Németh, K., 2012. Monogenetic Basaltic Volcanoes: Genetic Classification, Growth, Geomorphology and Degradation. INTECH Open Access Publisher.
Kereszturi, G., Németh, K., 2016. Sedimentology, eruptive mechanism and facies architecture of basaltic scoria cones from the Auckland Volcanic Field (New Zealand). J. Volcanol. Geotherm. Res. 324, 41–56.
Kereszturi, G., Németh, K., Cronin, S.J., Agustin-Flores, J., Smith, I.E.M., Lindsay, J., 2013. A model for calculating eruptive volumes for monogenetic volcanoes - implication for the Quaternary Auckland Volcanic Field, New Zealand. J. Volcanol. Geotherm. Res. 266, 16–33.
Kereszturi, G., Németh, K., Cronin, S.J., Procter, J., Agustín-Flores, J., 2014. Influences on the variability of eruption sequences and style transitions in the Auckland Volcanic Field, New Zealand. J. Volcanol. Geotherm. Res. 286, 101–115.
Kienle, J., Kyle, P.R., Self, S., Motyka, R.J., Lorenz, V., 1980. Ukinrek Maars, Alaska, I. April 1977 eruption sequence, petrology and tectonic setting. J. Volcanol. Geotherm. Res. 7 (1–2), 11–37.
Kokelaar, B.P., 1983. The mechanism of Surtseyan volcanism. J. Geol. Soc. 140 (6), 939–944.
Kokelaar, B.P., 1986. Magma-water interactions in subaqueous and emergent basaltic volcanism. Bull. Volcanol. 48 (5), 275–289.
Kokelaar, B.P., Durant, G.P., 1983. The submarine eruption and erosion of Surtla (Surtsey), Iceland. J. Volcanol. Geotherm. Res. 19 (3–4), 239–246.
Lautze, N.C., Houghton, B.F., 2007. Linking variable explosion style and magma textures during 2002 at Stromboli volcano, Italy. Bull. Volcanol. 69 (4), 445–460.
Le Corvec, N., Bebbington, M.S., Lindsay, J.M., McGee, L.E., 2013. Age, distance, and geochemical evolution within a monogenetic volcanic field: analyzing patterns in the Auckland Volcanic Field eruption sequence. Geochem. Geophys. Geosyst. 14 (9), 3648–3665.
LINZ - Land Information New Zealand, 2012. NZ 8 m Digital Elevation Model.
Lorenz, V., 1973. On the formation of maars. Bull. Volcanol. 37 (2), 183–204.
Lorenz, V., 1985. Maars and diatremes of phreatomagmatic origin; a review. S. Afr. J. Geol. 88 (2), 459–470.
Lorenz, V., 1986. On the growth of maar and diatremes and its relevance to the formation of tuff rings. Bull. Volcanol. 48 (5), 265–274.
Lorenz, V., 2003. Maar-diatreme volcanoes, their formation, and their setting in hard-rock or soft-rock environments. Geolines 15, 72–83.
Lorenz, V., 2007. Syn- and posteruptive hazards of maar-diatreme volcanoes. J. Volcanol. Geotherm. Res. 159 (1–3), 285–312.
Martin, U., Németh, K., 2004. Peperitic Lava Lake-Fed Sills at Sag-Hegy, Western Hungary: A Complex Interaction of a Wet Tephra Ring and Lava. In: Breitkreuz, C., Petford, N. (Eds.), Physical Geology of High-Level Magmatic Systems. Geological Society Special Publication, pp. 33–50.
Martin, U., Németh, K., 2005. Eruptive and depositional history of a Pliocene tuff ring that developed in a fluvio-lacustrine basin: Kissomlyó volcano (western Hungary). J. Volcanol. Geotherm. Res. 147 (3), 342–356.
Mattsson, H.B., 2010. Textural variation in juvenile pyroclasts from an emergent, Surtseyan-type, volcanic eruption: the Capelas tuff cone, São Miguel (Azores). J. Volcanol. Geotherm. Res. 189 (1), 81–91.
Mattsson, H.B., Höskuldsson, Á., 2011. Contemporaneous phreatomagmatic and effusive activity along the Hverfjall eruptive fissure, north Iceland: eruption chronology and resulting deposits. J. Volcanol. Geotherm. Res. 201 (1), 241–252.
McClelland, E., Erwin, P.S., 2003. Was a dacite dome implicated in the 9500 BP collapse of Mt Ruapehu? A palaeomagnetic investigation. Bull. Volcanol. 65 (4), 294–305.
McGetchin, T.R., Settle, M., Chouet, B.A., 1974. Cinder cone growth modeled after northeast crater, Mount Etna, Sicily. J. Geophys. Res. 79 (23), 3257–3272.
Möbis, A., 2010. Understanding the Holocene explosive eruption record of the Tongariro Volcanic Centre, New Zealand, Unpublished PhD thesis, Massey University, Palmerston North, 381 pp.
Moitra, P., Gonnermann, H.M., Houghton, B.F., Giachetti, T., 2013. Relating vesicle shapes in pyroclasts to eruption styles. Bull. Volcanol. 75 (2).
Moore, J.G., Nakamura, K., Alcaraz, A., 1966. The 1965 eruption of Taal volcano. Science 151 (3713), 955–960.
Murtagh, R.M., White, J.D., Sohn, Y.K., 2011. Pyroclast textures of the Ilchulbong 'wet' tuff cone, Jeju Island, South Korea. J. Volcanol. Geotherm. Res. 201 (1), 385–396.
Németh, K., 2010. Monogenetic volcanic fields: origin, sedimentary record, and relationship with polygenetic volcanism. Geol. Soc. Am. Spec. Pap. 470, 43–66.
Németh, K., Kereszturi, G., 2015. Monogenetic volcanism: personal views and discussion. Int. J. Earth Sci. 104 (8), 2131–2146.
Németh, K., Martin, U., Harangi, S., 2001. Miocene phreatomagmatic volcanism at Tihany (Pannonian Basin, Hungary). J. Volcanol. Geotherm. Res. 111 (1–4), 111–135.
Orsi, G., Gallo, G., Heiken, G., Wohletz, K., Yu, E., Bonani, G., 1992. A comprehensive study of pumice formation and dispersal: the Cretaio Tephra of Ischia (Italy). J. Volcanol. Geotherm. Res. 53 (1), 329–354.
Ort, M.H., Carrasco-Núñez, G., 2009. Lateral vent migration during phreatomagmatic and magmatic eruptions at Tecuitlapa Maar, east-central Mexico. J. Volcanol. Geotherm. Res. 181 (1–2), 67–77.

Pardo, N., Cronin, S.J., Palmer, A.S., Németh, K., 2012. Reconstructing the largest explosive eruptions of Mt. Ruapehu, New Zealand: lithostratigraphic tools to understand subplinian-plinian eruptions at andesitic volcanoes. Bull. Volcanol. 74 (3), 617–640.
Parfitt, E.A., 2004. A discussion of the mechanisms of explosive basaltic eruptions. J. Volcanol. Geotherm. Res. 134 (1–2), 77–107.
Pedrazzi, D., Aguire-Diaz, G., Bartolini, S., Marti, J., Geyer, A., 2014a. The 1970 eruption on Deception Island (Antarctica): eruptive dynamics and implications for volcanic hazards. J. Geol. Soc. 171 (6), 765–778.
Pedrazzi, D., Bolós, X., Martí, J., 2014b. Phreatomagmatic volcanism in complex hydrogeological environments: la Crosa de Sant Dalmai maar (Catalan Volcanic Zone, NE Spain). Geosphere 10 (1), 170–184.
Peslier, A.H., Luhr, J.F., 2006. Hydrogen loss from olivines in mantle xenoliths from Simcoe (USA) and Mexico: mafic alkalic magma ascent rates and water budget of the subcontinental lithosphere. Earth Planet. Sci. Lett. 242 (3), 302–319.
Putirka, K.D., 2008. Thermometers and barometers for volcanic systems. In: Putirka, K.D., Tepley, F. (Eds.), Minerals, Inclusions and Volcanic Processes. Reviews in Mineralogy and Geochemistry, pp. 61–120.
Price, R.C., Gamble, J.A., Smith, I.E., Maas, R., Waight, T., Stewart, R.B., Woodhead, J., 2012. The anatomy of an Andesite volcano: a time–stratigraphic study of andesite petrogenesis and crustal evolution at Ruapehu Volcano, New Zealand. J. Petrol., egs050
Pyle, D.M., 1989. The thickness, volume and grainsize of tephra fall deposits. Bull. Volcanol. 51 (1), 1–15.
Riedel, C., Ernst, G., Riley, M., 2003. Controls on the growth and geometry of pyroclastic constructs. J. Volcanol. Geotherm. Res. 127 (1), 121–152.
Sable, J.E., Houghton, B.F., Del Carlo, P., Coltelli, M., 2006. Changing conditions of magma ascent and fragmentation during the Etna 122 BCE basaltic Plinian eruption: evidence from clast microtextures. J. Volcanol. Geotherm. Res. 158 (3), 333–354.
Shea, T., Houghton, B.F., Gurioli, L., Cashman, K.V., Hammer, J.E., Hobden, B.J., 2010. Textural studies of vesicles in volcanic rocks: an integrated methodology. J. Volcanol. Geotherm. Res. 190 (3–4), 271–289.
Sheridan, M.F., Wohletz, K.H., 1981. Hydrovolcanic explosions: the systematics of water-pyroclast equilibration. Science 212 (4501), 1387–1389.
Sheridan, M.F., Wohletz, K.H., 1983. Hydrovolcanism: basic considerations and review. J. Volcanol. Geotherm. Res. 17 (1–4), 1–29.
Sohn, Y.K., Chough, S.K., 1989. Depositional processes of the Suwolbong tuff ring, Cheju Island (Korea). Sedimentology 36 (5), 837–855.
Son, M., Kim, J.S., Jung, S., Ki, J.S., Kim, M.-C., Sohn, Y.K., 2012. Tectonically controlled vent migration during maar–diatreme formation: an example from a Miocene half-graben basin in SE Korea. J. Volcanol. Geotherm. Res. 223, 29–46.
Sparks, R., Pinkerton, H., MacDonald, R., 1977. The transport of xenoliths in magmas. Earth Planet. Sci. Lett. 35 (2), 234–238.
Stovall, W.K., Houghton, B., Gonnermann, H., Fagents, S., Swanson, D., 2011. Eruption dynamics of Hawaiian-style fountains: the case study of episode 1 of the Kīlauea Iki 1959 eruption. Bull. Volcanol. 73 (5), 511–529.
Sumner, J.M., 1998. Formation of clastogenic lava flows during fissure eruption and scoria cone collapse: the 1986 eruption of Izu-Oshima Volcano, eastern Japan. Bull. Volcanol. 60 (3), 195–212.
Thorarinsson, S., 1965. Surtsey Eruption Course of Events and the Development of the New Island.
Tost, M., Cronin, S., 2015. Linking distal volcaniclastic sedimentation and stratigraphy with the development of Ruapehu volcano, New Zealand. Bull. Volcanol. 77 (11), 1–17.
Townsend, D.B., Vonk, A., Kamp, P.J.J., 2008. Institute of Geological and Nuclear Sciences 1:250 000 geological map 7. 1 sheet + 77 p. Lower Hutt, New Zealand, GNS Science.
Valentine, G.A., Cortés, J.A., 2013. Time and space variations in magmatic and phreatomagmatic eruptive processes at Easy Chair (Lunar Crater Volcanic Field, Nevada, USA). Bull. Volcanol. 75 (9), 1–13.
Valentine, G.A., Gregg, T.K.P., 2008. Continental basaltic volcanoes - processes and problems. J. Volcanol. Geotherm. Res. 177 (4), 857–873.
Valentine, G.A., White, J.D., 2012. Revised conceptual model for maar-diatremes: subsurface processes, energetics, and eruptive products. Geology 40 (12), 1111–1114.
Valentine, G., Perry, F., WoldeGabriel, G., 2000. Field characteristics of deposits from spatter-rich pyroclastic density currents at Summer Coon volcano, Colorado. J. Volcanol. Geotherm. Res. 104 (1), 187–199.
Vandergoes, M.J., Hogg, A.G., Lowe, D.J., Newnham, R.M., Denton, G.H., Southon, J., Barrell, D.J.A., Wilson, C.J.N., McGlone, M.S., Allan, A.S.R., Almond, P.C., Petchey, F., Dabell, K., Dieffenbacher-Krall, A.C., Blaauw, M., 2013. A revised age for the Kawakawa/Oruanui tephra, a key marker for the Last Glacial Maximum in New Zealand. Quat. Sci. Rev. 74, 195–201.
Vergniolle, S., Mangan, M.T., 2000. Hawaiian and Strombolian eruptions. In: Sigurdsson, H., Houghton, B.F., McNutt, S.R., Rymel, H., Stix, J. (Eds.), Encyclopedia of Volcanoes, pp. 447–461.
Walker, G.P.L., 1971. Grain-size characteristics of pyroclastic deposits. J. Geol. 696–714.
Walker, G.P.L., 1973. Explosive volcanic eruptions—a new classification scheme. Geol. Rundsch. 62 (2), 431–446.
White, J.D.L., 1996. Impure coolants and interaction dynamics of phreatomagmatic eruptions. J. Volcanol. Geotherm. Res. 74 (3), 155–170.
White, J.D.L., Ross, P.-S., 2011. Maar-diatreme volcanoes: a review. J. Volcanol. Geotherm. Res. 201 (1–4), 1–29.
Wilson, L., Head, J.W., 1981. Ascent and eruption of basaltic magma on the Earth and Moon. J. Geophys. Res. 86 (NB4), 2971–3001.
Wohletz, K.H., 1986. Explosive magma-water interactions: thermodynamics, explosion mechanisms, and field studies. Bull. Volcanol. 48 (5), 245–264.
Wohletz, K.H., McQueen, R.G., 1984. Experimental Studies of Hydromagmatic Volcanism, Explosive Volcanism: Inception, Evolution, and Hazards - Studies in Geophysics. National Academy Press, Washington, D.C., pp. 158–169.
Wohletz, K.H., Sheridan, M.F., 1983. Hydrovolcanic explosions II. Evolution of basaltic tuff rings and tuff cones. Am. J. Sci. 283 (5), 385–413.
Wohletz, K.H., Zimanowski, B., 2000. Physics of phreatomagmatism; I: explosion physics. Terra Nostra 6, 515–523.
Zellmer, G.F., Sakamoto, N., Iizuka, Y., Miyoshi, M., Tamura, Y., Hsieh, H.-H., Yurimoto, H., 2014. Crystal uptake into aphyric arc melts: insights from two-pyroxene pseudo-decompression paths, plagioclase hygrometry, and measurement of hydrogen in olivines from mafic volcanics of SW Japan. Geol. Soc. Lond. Spec. Publ. 385 (1), 161–184.
Zellmer, G.F., Sakamoto, N., Matsuda, N., Iizuka, Y., Moebis, A., Yurimoto, H., 2016. On progress and rate of the peritectic reaction Fo + SiO_2 → En in natural andesitic arc magmas. Geochim. Cosmochim. Acta 383–393.